Constraints on iron sulfate and iron oxide mineralogy from ChemCam visible/near-infrared reflectance spectroscopy of Mt. Sharp basal units, Gale Crater, Mars

Jeffrey Johnson, James Bell, Steve Bender, Diana Blaney, Edward Cloutis, Bethany Ehlmann, Abigail Fraeman, Olivier Gasnault, Kjartan Kinch, Stéphane Le Mouélic, et al.

LA-UR-17-27703 (Accepted Manuscript)

Constraints on iron sulfate and iron oxide mineralogy from ChemCam visible/near-infrared reflectance spectroscopy of Mt. Sharp basal units, Gale Crater, Mars

Johnson, Jeffrey R.; Bell, James F. III; Bender, Steve; Blaney, Diana; Cloutis, Edward; Ehlmann, Bethany; Fraeman, Abigail; Gasnault, Olivier; Kinch, Kjartan; Le Mouelic, Stephane; Maurice, Sylvestre; Rampe, Elizabeth; Vaiman, David; Wiens, Roger Craig

To be published in: American Mineralogist

DOI to publisher's version: 10.2138/am-2016-5553

Permalink to record: http://permalink.lanl.gov/object/view?what=info:lanl-repo/lareport/LA-UR-17-27703

Constraints on iron sulfate and iron oxide mineralogy from ChemCam visible/near-infrared reflectance spectroscopy of Mt. Sharp basal units, Gale Crater, Mars

Jeffrey R. Johnson[1], James F. Bell III[2], Steve Bender[3], Diana Blaney[4], Edward Cloutis[5], Bethany Ehlmann[4,6], Abigail Fraeman[6], Olivier Gasnault[7], Kjartan Kinch[8], Stéphane Le Mouélic[9], Sylvestre Maurice[7], Elizabeth Rampe[11], David Vaniman[3], Roger C. Wiens[10]

1—Johns Hopkins University Applied Physics Laboratory, Laurel, MD
2—Arizona State University, Tempe, AZ
3—Planetary Science Institute, Tucson, AZ
4—Jet Propulsion Laboratory, Pasadena, CA
5—University of Winnipeg, Winnipeg, Manitoba, Canada
6—California Institute of Technology, Pasadena, CA
7—Université de Toulouse, CNRS, Institut de Recherche en Astrophysique et Planetologie, Toulouse, France
8—University of Copenhagen, Niels Bohr Institute, Copenhagen, Denmark
9—Université de Nantes, Laboratoire de Planétologie et Géodynamique, Nantes, France
10—Los Alamos National Laboratory, Los Alamos, NM
11—Johnson Space Center, Houston, TX

Submitted to American Mineralogist
Special section on Mars mineralogy

September 5, 2015

ABSTRACT

Relative reflectance point spectra (400-840 nm) were acquired by the Chemistry and Camera (ChemCam) instrument on the Mars Science Laboratory (MSL) rover Curiosity in passive mode (no laser) of drill tailings and broken rock fragments near the rover as it entered the lower reaches of Mt. Sharp and of landforms at distances of 2-8 kilometers. Freshly disturbed surfaces are less subject to the spectral masking effects of dust, and revealed spectral features consistent with the presence of iron oxides and ferric sulfates. We present the first detection on Mars of a ~433 nm absorption band consistent with small abundances of ferric sulfates, corroborated by jarosite detections by the Chemistry and Mineralogy (CheMin) X-ray diffraction instrument in the Mojave, Telegraph Peak, and Confidence Hills drilled samples. Disturbed materials near the Bonanza King region also exhibited strong 433 nm bands and negative near-infrared spectral slopes consistent with jarosite. ChemCam passive spectra of the Confidence Hills and Mojave drill tailings showed features suggestive of the crystalline hematite identified by CheMin analyses. The Windjana drill sample tailings exhibited flat, low relative reflectance spectra, explained by the occurrence of magnetite detected by CheMin. Passive spectra of Bonanza King were similar, suggesting the presence of spectrally dark and neutral minerals such as magnetite. Long-distance spectra of the "Hematite Ridge" feature (3-5 km from the rover) exhibited features consistent with crystalline hematite. The Bagnold dune field north of the Hematite Ridge area exhibited low relative reflectance and near-infrared features indicative of basaltic materials (olivine, pyroxene). Light-toned layers south of Hematite Ridge lacked distinct spectral features in the 400-840 nm region, and may represent portions of nearby clay minerals and sulfates mapped with orbital near-infrared observations. The presence of ferric sulfates such as jarosite in the drill tailings suggests a relatively acidic environment, likely associated with flow of iron-

bearing fluids, associated oxidation, and/or hydrothermal leaching of sedimentary rocks. Combined with other remote sensing data sets, mineralogical constraints from ChemCam passive spectra will continue to play an important role in interpreting the mineralogy and composition of materials encountered as Curiosity traverses further south within the basal layers of the Mt. Sharp complex.

Keywords: Mars spectroscopy, Mars remote sensing, visible/near-infrared, IR Spectroscopy, ferric sulfates, iron oxides

INTRODUCTION

During the first 1000 martian days (sols) of operations the Mars Science Laboratory (MSL) rover Curiosity encountered a diverse array of stratigraphic settings within the 154 km diameter Gale Crater. These included ancient systems of groundwater networks, sporadic streams, and ephemeral lakes considered to represent potential habitable environments (Williams et al. 2013; Grotzinger et al. 2014, 2015a,b; Vasavada et al. 2014). Although the majority of the sediments associated with these alluvial, fluvial, and/or deltaic systems were largely composed of primary igneous minerals, detailed chemical and mineralogical analyses demonstrated that chemical weathering and/or diagenetic aqueous alteration occurred at a variety of pH levels (Schmidt et al. 2014; Sautter et al. 2014; Bish et al. 2014; Vaniman et al. 2014). Iron oxides, calcium and ferric sulfates, hydrated clay minerals, as well as substantial proportions of amorphous materials have been measured in drilled samples (Ming et al. 2014; Treiman et al. 2014; Vaniman et al. 2014; McClennan et al. 2014; Bish et al. 2014; Nachon et al. 2014; Bristow et al. 2015). Orbital mineralogical mapping of Gale Crater using visible/near-infrared reflectance spectroscopy also demonstrated that rock layers at the base of the ~ 5 km high Mt. Sharp (Aeolis Mons) contained appreciable amounts of clay minerals, sulfates, silica, and hematite, likely related to early climatic changes (Anderson and Bell 2010; Milliken et al. 2010; Grotzinger and Milliken 2012; Fraeman et al. 2013, Wray, 2013; Seelos et al. 2014). Indeed, the presence and distribution of ferric sulfates (such as jarosite) and iron oxides (such as hematite and magnetite) detected by Curiosity are particularly important in constraining the aqueous diagenetic history of rocks along the rover traverse, and the geochemical and temperature history of near-surface fluids that interacted with these rocks (e.g., Dixon et al. 2015).

During the MSL mission elemental composition has been obtained for in-situ samples using the Alpha Particle X-ray Spectrometer (APXS; Schmidt et al., 2013) and remotely using Laser-Induced Breakdown Spectroscopy (LIBS) with the Chemistry and Camera (ChemCam) instrument (e.g., Wiens et al. 2013, 2015). Mineralogy has been determined for a few drilled samples using the Chemistry and Mineralogy (CheMin) powder x-ray diffraction instrument. For the vast majority of rocks and soils not directly ingested by the rover's drilling and sampling system, additional constraints on mineralogy and composition were obtained using visible/near-infrared (VNIR) reflectance spectroscopy (400-1000 nm) with two complementary methods: point spectroscopy (400-840 nm) via the passive mode of ChemCam (Johnson et al. 2015), and multispectral imaging (445-1010 nm) from the Mastcam stereo camera system (Bell et al. 2013; Rice et al. 2013; Wellington et al. 2014). Because the MSL landing site region is relatively dusty (e.g., Seelos et al. 2014, Ehlmann and Buz 2015), many pristine surfaces exhibit VNIR spectra consistent with variable amounts of dust cover. However, freshly disturbed surfaces (drill tailing fines, areas subjected to rover wheels) are less subject to the masking effects of such dust.

In this paper we present ChemCam VNIR spectra of drill tailings and nearby exposed materials to demonstrate the presence of iron oxides such as hematite and magnetite, and we document the first detection on Mars of the ~433 nm absorption band associated with ferric sulfates. We also present long-distance results that demonstrate the capability to detect hematite and variable spectral properties of outcrop and dune materials several kilometers away. We compare ChemCam spectra to laboratory spectra of various minerals and to mineralogical results from CheMin (e.g., Bish et al. 2014; Downs et al. 2015). In a companion paper, Wellington et al. (this issue) present Mast Camera (Mastcam) multispectral imaging results for similar targets, employing the longer wavelengths and greater spatial coverage provided by Mastcam.

BACKGROUND

VNIR Spectroscopy

Visible/near-infrared (400-1000 nm) spectra provide a valuable means of constraining mineralogy and crystallinity of iron-bearing minerals on Mars and in the laboratory (e.g., Singer et al. 1979; Morris et al., 2000; Bell et al. 2000, 2008; Johnson et al. 2007; Ehlmann and Edwards, 2014). A decrease in reflectance towards the near-infrared is attributable to the presence of Fe^{2+} absorption bands associated with mafic silicate minerals such as pyroxenes and olivine (e.g., Roush et al. 1993). Absorptions from Fe^{3+} cause strong, positive slopes from the blue to red wavelengths, with relative reflectance maxima typically near 750 nm. Ratios of red/blue wavelengths provide first-order information on the relative level of oxidation of surface materials and/or degree of dust coatings on martian surfaces (e.g., Johnson and Grundy 2001; Johnson et al. 2003). Relatively dust-free "gray" rocks observed by in situ multispectral imagers on Mars exhibit lower red/blue color ratios than more dust-coated surfaces (McSween et al. 1999; Bell et al. 2004a,b; Farrand et al. 2006, 2007, 2008a,b; Wellington et al, this issue). The strength of the short wavelength Fe^{3+} absorption edge can be determined by the spectral curvature near 600 nm. Absorptions near 535 nm and in the 800-1000 nm region are consistent with the presence of crystalline ferric oxides such as hematite (Morris et al. 1985, 1997, 2000; Bell et al. 2004a,b;). Ferric sulfates such as jarosite, coquimbite, and rhomboclase also exhibit absorption bands near 433 nm, sometimes with weaker 530, 790, and/or ~870 nm bands (Bishop and Murad, 1996; Bishop et al. 2015; Johnson et al. 2007; Lane et al. 2008). The ~433 nm band is related to the $^6A_{1g}$-($^4A_{1g}$,^4E_g) ferric iron spin-forbidden crystal field transition, where the shape and position of this band are related to the distortion of the iron octahedra (Rossman et al. 1975;

127 Sherman et al. 1982; Cloutis et al. 2006a, 2008; McCollom et al. 2014; Sklute et al. 2015) and to
128 a lesser extent grain size (Pitman et al. 2014).

129 **ChemCam Passive Spectroscopy**

130 The LIBS portion of the ChemCam instrument disperses light emitted from a laser-
131 generated plasma onto three spectrometers to detect elemental emission lines at high spectral (<
132 1 nm) and spatial (0.65 mrad FOV) resolution (Wiens et al. 2013, 2015). Johnson et al. (2015)
133 demonstrated that although the ChemCam "violet" (VIO, 382-469 nm) and visible/near-infrared
134 (VNIR, 474-906 nm) spectrometers were not designed for reflectance spectroscopy, they
135 exhibited sufficient sensitivity to allow collection of useful surface spectral reflectance in passive
136 mode (i.e., without using the laser). Johnson et al. (2015) presented relative reflectance spectra
137 (400-840 nm) of rocks, dust, and soils near the rover (~2-7 m) acquired during the first 360 sols,
138 where spatial resolutions of the point locations ranged from 1.3-4.5 mm. Analyses of the band
139 depths, spectral slopes, and ratios among these spectra revealed six spectral endmembers
140 characterized by variations in ferrous and ferric components. For example, "exposed" materials
141 (brushed or freshly broken surfaces) exhibited low 535 nm band depths and low 670/440 nm
142 ratios, indicative of the less oxidized nature of these more ferrous materials relative to, e.g.,
143 Martian dust. Typical reddish, oxidized, dusty surfaces exhibited similarities to palagonite-rich
144 soils. "Dark" float rocks exhibited low relative reflectance and significant downturns longward
145 of 700 nm that were consistent with the presence of orthopyroxene. Magnesium-rich "raised
146 ridges" tended to exhibit distinct, negative near-infrared slopes. Calcium-sulfate veins exhibited
147 the highest relative reflectances, but were still relatively red owing to the effects of dust and/or
148 minor structural Fe^{3+} contamination. Such dust was less prominent on rocks within the "blast

zone" surrounding the Bradbury landing site. These samples were likely affected by the landing thrusters, which partially removed the ubiquitous dust coatings.

METHODOLOGY

For every LIBS point measurement acquired by ChemCam with its laser, a 3 msec exposure passive ("dark") measurement is acquired without the laser for calibration purposes. As shown by Johnson et al. (2015) these "dark" measurements are of sufficient quality to be used as passive radiance spectra when acquired on sunlit surfaces. Longer exposure ("dedicated") measurements at 30 msec were acquired when possible for specific targets of interest to increase the signal to noise ratio (SNR). Calibration of such measurements to relative reflectance followed procedures similar to those established for field spectroscopy (e.g., Johnson et al. 2001; Milton et al. 2009), in which a scene radiance spectrum is divided by a calibration target radiance spectrum. We used observations acquired at 3 msec and 30 msec exposures on Sol 76 of the white ChemCam calibration target holder to minimize dark current variations between scene and calibration targets. We converted the raw data to radiance using the methods described by Johnson et al. (2015). The ratio of the scene and calibration target radiance measurements, multiplied by the known laboratory reflectance of the calibration target material (Wiens et al. 2013), provided an estimate of relative reflectance. Johnson et al. (2015) estimated that the radiance absolute calibration uncertainty was 6-8%. They noted that even with moderate relative reflectance uncertainties (e.g., 20-30%), the band positions and shapes were resilient to calibration errors and ultimately useful in constraining compositions and/or mineral detections.

Remote Micro-Imager (RMI) images were acquired as part of ChemCam observations, from which accurate locations for the individual points within a raster could be placed (Wiens et

al. 2012, 2015; Maurice et al. 2012; Le Mouélic et al. 2015). Comparison to Mastcam M-100 images acquired as part of the ChemCam observations also provided context images for interpreting the passive spectra. The 0.65 mrad FOV of the spectra corresponds to a ~ 2mm spot size at an observation distance of 3 mm. Longer-distance observation effective FOVs are subject to minor, variable elongation resulting from the projection of the FOV onto local topography.

Analyses of the spectra benefited from the use of spectral parameters calculated using ±5 nm averages around a central wavelength. In the visible wavelengths, 670/440 nm ratios are sensitive to oxidation state and/or dust deposition, whereas in the near-infrared region slopes from 750 nm to 840 nm and 600 nm to 840 nm are indicative of the strength of iron absorptions. The 600 nm band depth (shoulder) is sensitive to the strength of the short wavelength ferric oxide absorption edge, and was calculated with a continuum between 535 nm and 670 nm. The 535 nm band depth is sensitive to the presence of crystalline ferric oxides (e.g., Morris et al. 1997, 2000) and was calculated with a continuum between 500 nm and 600 nm (cf. Bell et al. 2000).

DATA SETS

The primary data sets used here and their observation sequence identifications are listed in Table 1. They include representative samples of the drill tailings from Cumberland (at Yellowknife Bay), Windjana (at The Kimberley), and the triad of samples collected in the Pahrump Hills area (in stratigraphic order, upsection: Confidence Hills, Mojave, and Telegraph Peak). Figure 1b shows their locations on a rover traverse map, in addition to two targets of interest near Hidden Valley: Bonanza King and Perdido2. All spectra examined here were acquired with dedicated 30 msec exposures except for 3 msec exposures (used as part of the standard LIBS passive background measurements) for Cumberland, Windjana, and Confidence

195 Hills. Also listed in Table 1 are long distance passive spectra sequences acquired of landforms
196 2-8 km south of the rover's traverse. These areas encompassed dark-toned, dominantly basaltic
197 dunes, hematite-bearing materials on the region informally known as Hematite Ridge (Fraeman
198 et al. 2013), fan-like materials occurring near the base of Mt. Sharp (Figure 1a), and nearby light-
199 toned mounds. Table 1 also includes the atmospheric opacity values calculated from Mastcam
200 observations at 880 nm using the techniques of Lemmon et al. (2004), as well as the time of day
201 and phase angle of the observations.

202 **Drill Tailings and Disturbed Materials**

203 **Cumberland**. The two drill samples acquired at Yellowknife Bay were John Klein and
204 Cumberland. CheMin results showed each to have similar mineralogy in their crystalline
205 components with dominantly plagioclase feldspar (22 wt%), pyroxene (16 wt%), clay minerals
206 (~20% trioctahedral smectites), magnetite (4 wt%), minor calcium sulfates, iron
207 oxide/hydroxides, and Fe-sulfides, and ~30 wt% amorphous materials (e.g., Vaniman et al.
208 2014). Although the passive spectra of each drill sample were essentially identical, the
209 Cumberland data were acquired earlier in the day (at lower detector temperatures) and therefore
210 exhibited slight better SNR. As such, we used the Cumberland data from Sol 289 in this work.

211 **Windjana**. Figure 2 shows the RMI image and location of 8 raster points acquired on Sol 619
212 of the Windjana mini-drill tailings in The Kimberley region (cf. Fig. 1a). The full drill tailings
213 (shown in the accompanying Mastcam image) exhibited identical reflectance properties.
214 CheMin results for the Windjana crystalline components were modeled as augite (20 wt%),
215 pigeonite (10 wt%), olivine (5 wt%), monoclinic sanidine (20 wt%), plagioclase (4 wt%)
216 magnetite (12 wt%), phyllosilicate (8 wt%), and amorphous /poorly crystalline phases (15-20
217 wt%). (e.g., Downs et al. 2015; Treiman et al. 2015a,b).

Bonanza King and Perdido2. Near the entrance to Hidden Valley drilling was attempted on the Bonanza King target, but abandoned after the target became unstable during the mini-drill attempt (Anderson et al. 2015b). Figure 3 includes the Sol 726 RMI mosaic showing the locations of a 4x4 raster and the Mastcam image of this disturbed area. Although no CheMin analyses were obtained of this material, the APXS and ChemCam LIBS data indicated a dominantly basaltic composition with minor calcium sulfates. Compared to Windjana and the Yellowknife Bay samples, the Fe and Mg were lower, Si higher, with an unusually high amount of P (P_2O_5~2%) (Thompson et al. 2015). While at this location ChemCam 3 msec passive spectra were acquired of a freshly broken rock fragment named Perdido that suggested interesting spectral features. Therefore, a dedicated passive raster (30 msec exposures) at the same location was collected on Sol 728. Figure 4 shows the RMI and Mastcam images of these targets, in which the 5th location of the passive raster was located on the surface of a broken fragment named Perdido2.

Confidence Hills. At Pahrump Hills the Confidence Hills drill tailings were observed on Sol 762 after the full drilling was completed. Figure 5 shows the 1x10 raster on the RMI mosaic and accompanying Mastcam image of the target Stovepipe Wells, where locations #4 through #10 were located on the drill tailings. CheMin crystalline phases include plagioclase (26 wt%), augite (7 wt%), pigeonite (7 wt%), forsterite (<1 wt%), hematite (8 wt%), magnetite (4 wt%), potassium feldspar (6 wt%), phyllosilicate (10 wt%), minor (~1 wt %) cristobalite, ilmenite, jarosite, and quartz, and amorphous material comprising 26 wt% of the sample (cf. Cavanagh et al. 2015; Rampe et al. 2015a).

Mojave. The mini-drill attempt at Mojave was partially successful, as evidenced by Figure 6, which shows an RMI mosaic and 1x5 dedicated passive raster acquired on Sol 869 with an

241 accompanying Mastcam image. Raster location #1 hit a small fragment of freshly dislodged
242 material from Mojave. (Additional 3 msec "dark" passive measurements were acquired on the
243 ultimate drill hole tailings on Sol 883. However, the relatively thin tailings pile was partially
244 removed by the LIBS laser blasts and the associated passive data are not used here.) CheMin
245 results from the nearby full drill analysis showed the sample to contain plagioclase (28 wt%),
246 augite (2 wt%), pigeonite (7 wt%), magnetite/maghemite (4 wt%), hematite (3 wt%), jarosite (4
247 wt%), apatite (3 wt%), phyllosilicate (6 wt%), minor (~1 wt %) ilmenite and quartz, and 42 wt%
248 amorphous materials (cf. Rampe et al. 2015a,b).

249 **Telegraph Peak**. Figure 7 shows a RMI mosaic and locations of a 5x1 raster on the full drill
250 hole at Telegraph Peak acquired on Sol 910 along with the Mastcam image. CheMin results
251 from a nearby full drill analysis showed the sample to contain plagioclase (30 wt%), potassium
252 feldspar (5 wt%), orthopyroxene (4 wt%), pigeonite (5 wt%), magnetite/maghemite (9 wt%),
253 cristobalite (7 wt%), jarosite (2 wt%), apatite (3 wt%), no phyllosilicates, augite, and minor (~1
254 wt %) olivine, hematite, ilmenite and quartz, , with 31 wt% amorphous materials (cf. Rampe et
255 al. 2015b).

256 **Long Distance Observations.**

257 The relatively low atmospheric opacity ($\tau < 0.65$) that occurred during Sols 432-492 (L_s
258 40-67°) was exploited to test the long-range capability of ChemCam passive spectra by acquiring
259 observations on targets up to 8 km from the rover (Table 1). These included portions of the
260 Bagnold Dune region south of the rover, the Hematite Ridge (HR) area, a "fan" region south of
261 Hematite Ridge (referred to by Grotzinger et al. (2015b) as part of a "draping strata" unit) and
262 underlying light-toned materials (Fig. 1a). As an example of these data sets, Figure 8 shows a
263 Mastcam false-color image with outlines designating the locations of two RMI mosaics

associated with ChemCam passive 1x10 rasters acquired on Sol 467 (described further below). Light-toned mounds at the base of the "fan" materials were observed on Sol 492 along with the top of Hematite Ridge, as shown in Figure 9.

RESULTS

Overview of spectral features and parameters

Representative spectra from the samples are displayed in Figure 10. The Windjana drill tailings exhibit the lowest relative reflectance and a relatively flat spectrum, consistent with the magnetite detected by CheMin. By comparison, the Confidence Hills spectrum (Stovepipe Wells target) shows a deep ~535 nm absorption band and a near-infrared falloff that occurs near 785 nm, consistent with the hematite detected by CheMin (Table 2). A weak 433 nm absorption band is consistent with the presence of minor jarosite as well. The presence of the 433 nm band is somewhat more distinct in the Bonanza King spectrum, which is otherwise one of the flattest spectra observed by ChemCam. The lack of appreciable slopes in this spectrum suggests a relatively large amount of a spectrally neutral material such as magnetite. For comparison, Telegraph Peak shows a similarly flat spectrum and was found by CheMin to contain ~10 wt% magnetite. The minor 433 nm band in Telegraph Peak is also consistent with the 2 wt% jarosite detected by CheMin, and suggests that a similar amount is likely present in Bonanza King. The Perdido2 broken fragment demonstrates the deepest 433 nm band yet observed by ChemCam, along with one of the deepest near-infrared falloffs, beginning near 700 nm. These features are consistent with significant jarosite at this location, as demonstrated in more detail below.

The Mojave spectrum has a slightly shallower ~535 nm band than the Stovepipe Wells target on Confidence Hills (and correspondingly lower hematite content from CheMin). Mojave has twice the weight percent of jarosite than Telegraph Peak according to CheMin results, and its

433 nm band is correspondingly deeper. However, the Stovepipe Wells spectrum exhibits a 433 nm band of intermediate depth, despite it having the lowest jarosite content among these three sites (Table 3). Furthermore, even the jarosite-free Cumberland sample's spectrum suggests a nearly equivalent calculated 433 nm band depth, and the low reflectance Windjana spectrum's 433 nm band depth is even larger. These "false-positives" may result from additional noise in this spectral region arising from the shorter exposure (3 msec) used for these two locations compared to the other two samples (Table 3). It also illuminates the difficulty in linearly correlating spectral band depths with abundance in the visible region of the spectrum, particularly when opaque phases such as magnetite are present.

Figure 11 compares some of the key visible and near-infrared spectral parameters among the drill tailing spectra (including spectra from additional raster locations from the sequences listed in Table 1). The Confidence Hills spectrum (Stovepipe Wells) exhibits the largest 535 nm band depth and most negative 600 nm band depth (consistent with the presence of hematite), whereas the less oxidized Cumberland tailings exhibit the lowest 535 nm band depths (Fig. 11a). The flat spectra of Bonanza King and Telegraph Peak result in their low 670/440 nm ratios and high 600 nm band depths (Figs. 11a-b). Comparison of the 600/840 nm ratio and slopes (Fig. 11c) reveals a continuum of values ranging from low ratios and high slopes in the more oxidized Confidence Hills sample to the high ratios and low slopes associated with less oxidized Bonanza King. The location of Windjana parameters slightly below this trend is likely related to slightly greater shadowing of the surface related to the higher phase angle (Table 1, Fig. 2, cf. Johnson et al. 2015). Finally, the 750 to 840 nm slopes are least negative for Windjana (Fig. 11d), consistent with their low relative reflectance and moderately flat spectra.

Comparison to laboratory spectra

In Figure 12 laboratory spectra of jarosite, ferricopiapite, and natrojarosite are plotted with the Perdido2 spectrum (multiplied by 3.25 for ease of comparison). These ferric sulfates exhibit similar, relatively narrow absorption bands near 433 nm and a downturn at wavelengths less than about 410 nm. They also show pronounced downturns in reflectance at wavelengths greater than about 700 nm. The ~433 nm feature has been observed in laboratory and terrestrial field work but never on Mars (e.g., Cloutis et al. 2006a; McCollom et al. 2014, Sobron et al. 2014; Sklute et al. 2015). McCollom et al. (2014) demonstrated that this feature is more apparent at low Fe# (= 100 × Fe/(Al+Fe) on a molar basis). Figure 12 shows two of their natrojarosite spectra with Fe# values of 10 and 20. The ChemCam LIBS spectra acquired on Sol 725 of the nearby Perdido target (the block directly above raster location #5 in Figure 4) reveal average contents for Fe (19.9 wt %) and Al (11.1 wt %), which corresponds to an intermediate Fe# (~46). Although it is unlikely that each LIBS location sampled only pure ferric sulfate, this intermediate Fe# may be one reason that the 433 nm band depth of Perdido2 (0.071; Table 3) is less than that for the lab spectra in Figure 12 (e.g., 0.310 for the jarosite spectrum).

Figure 13 shows laboratory spectra of ferric oxides compared to the Confidence Hills (Stovepipe Wells) and Mojave spectra (contrast-enhanced to facilitate comparisons). Although spectral features in the ChemCam spectra are subtle, the absorption near 535 nm and the flat region near 660 nm are distinct from typical passive spectra. Combined with the minor spectral downturn > 750 nm, these features are all consistent with a combination of crystalline and/or nanophase hematite. Contributions from other crystalline or poorly crystalline hydroxylated Fe(III) oxides (e.g., maghemite, ferrihydrite, and magnetite) or sulfates (e.g., schwertmannite) cannot be excluded and may be indicated by the small shifts in spectral maxima and minima relative to the hematite endmember. Nonetheless, for those iron oxides deemed above the

detection limits CheMin reported ~4 wt% magnetite and 3 wt% hematite in Mojave and 4 wt% magnetite and 8 wt % hematite in Confidence Hills (Table 2; Cavanagh et al. 2015; Rampe et al. 2015b).

Long-distance spectra

Two examples from the long distance experiments are presented in Figure 14. The HR1 region (Fig. 14a) included targets in the near field (locations #1-3) consistent with typical dusty martian areas. Locations #4, 5, and 8 fell on predominantly dark dune materials and exhibited the lowest relative reflectance spectra, with gradual downturns at wavelengths greater than about 750 nm, consistent with mafic materials (olivine, pyroxene) in the dune sands. However, locations on Hematite Ridge (#6, 7, 9, and 10) exhibited flatter spectra in the ~660 nm region, a perceptibly deeper ~535 nm band, and a steeper downturn > 750 nm. As with the Confidence Hills spectra, these features are also consistent with small amounts of crystalline hematite associated with Hematite Ridge and similar nearby materials. Similar results were found for the HR2 region, where dune materials in locations #4, 5, and 8 exhibited spectra distinct from the locations on Hematite Ridge (#6 and 10), particularly in the near-infrared, again consistent with hematite (Fig. 14b).

Figure 15 shows the results of targeting the light-toned mounds that occur near the base of the "fan" materials to the south of Hematite Ridge. In this raster, the hematite-bearing regions correspond to locations #3, 4 and 5 and exhibited the same features described above. The dune materials were sampled by locations #7, 8, and 9, whereas the "fan" material is represented by location #10 and exhibited a similar spectral shape to the dunes but a higher relative reflectance. This may result from a slightly smaller grain size of the materials comprising the "fan" and/or a photometric effect. Location #6 sampled the light-toned mound itself, but other than a distinctly

high relative reflectance there are no diagnostic spectral features other than the typical ferric absorption edge associated with martian dust. This could be consistent with the presence of phyllosilicate-bearing and/or sulfate minerals, given their typically neutral spectra in this wavelength region.

The results of all long-distance observations (Table 1) are summarized in Figure 16 by comparing spectral parameters similar to those used in Figure 11 as well as the 750 nm inflection (band depth). For each data set in Figure 16 the raster location numbers are shown next to each symbol. Based on comparing spectral features and their locations in RMI images, outlines were drawn around distinctive spectral parameter regions associated with five unit types: dunes, "fan" materials, typical dusty foreground regions, hematite-like areas, and the light-toned mound. The typical dusty foreground areas exhibit nearly flat 750 nm to 840 nm slopes, large 670 nm to 440 nm (red-blue) slopes, and among the smallest 750 nm band depths. By comparison, the dune materials exhibit small 535 nm band depths, more negative near-infrared slopes, and the lowest red-blue slopes. The "fan" materials fall within the spectral parameter space of the dunes, but at relatively low 535 nm and 750 nm band depths and high 670 nm to 440 nm slopes. The light-toned mound areas are relatively distinct with their large red-blue slopes. The hematite-like materials exhibit the largest 535 nm band depths and most negative near-infrared slopes and 750 nm band depths, with relatively high red-blue slopes.

DISCUSSION

ChemCam passive spectra provide a complementary perspective on the occurrence of iron-bearing minerals in drill tailings, freshly disturbed surfaces, and relatively dust-free areas that is consistent with results from other instruments. As a reconnaissance tool to investigate areas worthy of detailed in situ investigations, these unique data add value to other remote

sensing observations that use LIBS spectra and Mastcam multispectral data (Jackson et al., 2015; Wellington et al. 2015, this issue). Among the spectra investigated here, hematite-bearing materials are evident in the Confidence Hills and Mojave materials, consistent with CheMin results (Table 2). Hematite-bearing spectra were also observed in multiple long-distance observations near and on materials associated with Hematite Ridge, consistent with CRISM orbital observations (Milliken et al. 2010; Fraeman et al. 2013, 2015). Similarly, observations of the dark dune materials south of the rover exhibited long-distance spectra indicative of the presence of olivines and/or pyroxenes, consistent with CRISM observations (Seelos et al. 2014; Ehlmann and Buz, 2015; Lapotre et al. 2015).

The low reflectance, spectrally flat nature of magnetite has a nonlinear contribution to spectra in the visible wavelength region (Cloutis et al. 2011), and was considered a viable candidate for the Windjana and Telegraph Peak drill tailings prior to their sample analyses. The 9-12 wt% magnetite abundances determined for both samples by CheMin (Table 2) were consistent with these predictions. The similarity between Telegraph Peak and Bonanza King spectra (Fig. 10) suggests that the latter has a similar contribution from magnetite (or other minerals with dark, neutral spectra such as ilmenite). Moreover, the ~3-4 wt% magnetite abundance determined by CheMin in the other drill samples (Table 2) provided a darkening agent in those samples that contributed to relative reflectance values that are moderate for Mars (typically below 0.25).

The presence of a 433 nm absorption band agrees with the CheMin detection of jarosite in the Mojave, Telegraph Peak, and Confidence Hills drill tailings (Table 2). We interpret the combination of a deep 433 nm band in the Perdido2 target spectrum and the strong decrease in relative reflectance at wavelengths > 700 nm to represent a significant contribution from ferric

sulfate in that target, for which CheMin mineralogy data were not acquired. Because calculation of 433 nm band depths was subject to band-to-band noise in the ChemCam VIO detector, attempts to correlate band depth with ferric sulfate abundance were inconsistent, even when averaging over 5 nm intervals (Table 3). Nonetheless, comparison of spectra shown in Figure 10 suggests that ferric sulfates such as jarosite are a likely component of the Bonanza King materials as well. This emphasizes how the iterative interpretations of ChemCam passive spectra with CheMin mineralogy can be used to expand interpretations of remotely-sensed observations and enhance the predictive capability of such reconnaissance observations. Adding observations from other payload elements such as Mastcam multispectral imaging and ChemCam and APXS elemental chemistry can also assist with interpretations of detailed variations, as explored by Wellington et al. (2015) and Jackson et al. (2015).

At the Pahrump Hills locality, Confidence Hills is the stratigraphically lowest drilled sample, at the bottom of the Pahrump Member of the Murray Formation, followed by Mojave and Telegraph Peak near the top (Stack et al., 2015; Grotzinger et al. 2015b). The decrease in hematite and increase in magnetite concentrations from Confidence Hills to Telegraph Peak suggests that reducing conditions were more prevalent higher in the sequence. The additional presence of ferric sulfates such as jarosite suggests a relatively acidic environment, at least during some (perhaps limited) time in the past. In situ diagenetic processes likely occurred with variable pulses of iron-bearing fluids and associated oxidation, possibly aided by leaching of sedimentary rocks via hydrothermal processes. There also could have been a combination of relatively pristine components mixed with a different source that was more chemically weathered (McClennan et al. 2015). In terrestrial settings, changes in the redox state can occur without significant changes to the bulk chemistry of the constituent materials, and can occur erratically

425 over short spatial distances (as observed in some of the mm-scale observations investigated
426 here). Tracking the occurrence of these minerals throughout the rover traverse is therefore an
427 important part of understanding the geochemical and spatial evolution of materials near the base
428 of Mt. Sharp.

429 **IMPLICATIONS**

430 The methods developed by Johnson et al. (2015) to use the ChemCam instrument as a
431 passive reflectance spectrometer afford the opportunity to enhance the science return from the
432 Curiosity rover by providing additional constraints and spatial sampling of the mineral diversity
433 along the rover's traverse. Although variable surface dust subdues many spectral features in the
434 400-840 nm wavelength region, drill tailings, freshly disturbed materials, and relatively dust-free
435 (e.g., wind-abraded) samples provide the opportunity to investigate with greater spectral contrast
436 the band positions, shapes, depths and spectral slopes of passively collected ChemCam spectra.
437 The ChemCam relative reflectance spectra presented here include the first documented evidence
438 for the presence of an absorption band near 433 nm in spectra of in situ martian materials.
439 Combined with a spectral downturn longward of 700 nm, these spectra are consistent with
440 detections of a ferric sulfate such as jarosite (e.g., Cloutis et al. 2006a; McCollom et al.; 2014,
441 Sobron et al. 2014; Sklute et al. 2015). Additionally, enrichments in ferric oxides such as
442 hematite have been identified in select drill tailings as well as in landscape-scale features higher
443 on Mt. Sharp.

444 Mineralogical constraints from ChemCam passive spectra are important to daily
445 operations of the rover and targeting of potential in situ analysis locations, particularly when
446 combined with other remote sensing data sets. For example, this information can be used as an
447 additional means of deciphering the chemostratigraphy and mineralogy of rock facies observed

along the traverse (e.g., Vaniman et al. 2014; Anderson et al. 2015a; Fraeman et al. 2013; Mangold et al. 2015), variations in igneous mineralogy (e.g., Stolper et al. 2013; Sautter et al. 2014; Schmidt et al. 2014), compositional and mineralogical variability related to grain size in soils and rocks (e.g., Blake et al. 2013; Cousin et al. 2015), the effects of coatings (e.g., Lanza et al. 2015), and geochemical observations and models of secondary mineral formation (e.g., McLennan et al. 2014; Blaney et al. 2014; Treiman et al. 2014; Bridges et al. 2015; Bristow et al. 2015). Long-distance observations are useful for strategic planning of possible traverse routes and future targets (e.g., Vasavada et al. 2014; Fraeman et al. 2015).

Based on these results, ongoing rover in situ and long-distance observations of the lower portions of Mt. Sharp will continue to reveal spectral variations attributable to variable proportions of hematite, magnetite, ferric sulfates, iron-bearing clay minerals, and perhaps other mixed occurrences of ferrous and ferric materials. Fresh materials (drill tailings, disturbed rocks) will likely have the greatest potential to reveal spectral variations less contaminated by the variable masking effects of dust coatings. Outcrops higher up on Mt. Sharp that exhibit spectral and mineralogical variations visible to CRISM will also likely continue to prove fruitful targets for ChemCam passive observations, helping guide the rover's path and contextualize other science data. Investigations of the active and inactive portions of the barchan and longitudinal dunes of the Bagnold dune field south of the rover should provide additional constraints on the mineralogical variability of dune sands (Lapotre et al. 2015). The capability of the rover's sampling system to generate and place on the surface two to three sieved, grain size separates may provide the opportunity to investigate compositional variability as a function of grain size within the sands.

Ongoing analyses of ChemCam passive spectra will continue to provide valuable experience with rover-based visible/near-infrared point spectroscopy that will be valuable for the upcoming Mars2020 mission. The SuperCam instrument selected as a payload element on that rover will include combined LIBS, Raman, and visible/near-infrared (~400-900 nm) point spectroscopy. In addition, the 1300-2600 nm region will be sampled by a separate spectrometer where the light is dispersed sequentially by an acousto-optical tunable filter (Maurice et al. 2015; Fouchet et al. 2015). Combined use of those techniques with multispectral imaging from the Mastcam-Z payload element on Mars2020 (Bell et al. 2014) will provide compositional and mineralogical reconnaissance information vital to selecting targets to sample, drill, and cache for eventual sample return.

ACKNOWLEDGMENTS

This work was funded by the NASA Mars Science Laboratory Participating Scientist program through the Jet Propulsion Laboratory (contract 1350588). The US portion of ChemCam and MSL rover operations was funded by NASA's Mars Exporation Program. The French contribution to MSL is supported by the Centre National d'Etudes Spatiales (CNES). Work by K. Kinch was supported by the Danish Council for Independent Research/Natural Sciences (FNU grant 12-127126). A. Fraeman is supported by Keck Institute for Space Studies and Caltech GPS division Texaco postdoctoral fellowships. The authors thank W. Farrand and an anonymous reviewer for their helpful suggestions, and to J. Bishop for valuable editorial recommendations.

REFERENCES CITED

Anderson, R.B., and Bell, J.F. III (2010) Geologic mapping and characterization of Gale crater and implications for its potential as a Mars Science Laboratory landing site. Mars, 5, 76–128.

Anderson, R., J.C. Bridges, A. Williams, L. Edgar, A. Ollila, J. Williams, M. Nachon, N. Mangold, M. Fisk, J. Schieber, S. Gupta, G. Dromart, R. Wiens, S. Le Mouélic, O. Forni, N. Lanza, A. Mezzacappa, V. Sautter, D. Blaney, B. Clark, S. Clegg, O. Gasnault, J. Lasue, R. Léveillé, E. Lewin, K.W. Lewis, S. Maurice, H. Newsom, S.P. Schwenzer, and D. Vaniman (2015a) ChemCam results from the Shaler outcrop in Gale Crater, Mars, Icarus, 249:2-21, doi:10.1016/j.icarus.2014.07.025.

Anderson, R. C., Beegle, L., & Abbey, W. (2015b). Drilling on Mars: What We Have Learned from the Mars Science Laboratory Powder Acquisition Drill System (PADS). In Lunar and Planetary Science Conference, abstract# 2417.

Bell, J.F. III, H. Y. McSween, Jr., S.L. Murchie, J.R. Johnson, R. Reid, R.V. Morris, R.C. Anderson, J.L. Bishop, N.T. Bridges, D.T. Britt, J.A. Crisp, T. Economou, A. Ghosh, J.Greenwood, H.Gunnlaugsson, R.M. Hargraves, S. Hviid, J.M. Knudsen, M.B. Madsen, H.J. Moore, R. Rieder, and L. Soderblom (2000) Mineralogic and compositional properties of martian soil and dust: Preliminary results from Mars Pathfinder, Journal of Geophysical Research, 105, 1721-1755.

Bell III, J.F., S.W. Squyres, R.E. Arvidson, H.M. Arneson, D. Bass, D. Blaney, N. Cabrol, W. Calvin, J. Farmer, W.H. Farrand, W. Goetz, M. Golombek, J.A. Grant, R. Greeley, E. Guinness, A.G. Hayes, M.Y.H. Hubbard, K.E. Herkenhoff, M.J. Johnson, J.R. Johnson, J. Joseph, K.M. Kinch, M.T. Lemmon, R. Li, M.B. Madsen, J.N. Maki, M. Malin, E. McCartney, S. McLennan, H.Y. McSween, Jr., D.W. Ming, J.E. Moersch, R.V. Morris, E.Z. Noe Dobrea, T.J. Parker, J. Proton, J.W. Rice, Jr., F. Seelos, J. Soderblom, L.A. Soderblom, J.N. Sohl-Dickstein, R.J. Sullivan, M.J. Wolff, and A. Wang (2004a) Pancam multispectral imaging results from the Spirit rover at Gusev crater, *Science, 305,* 800-806.

Bell III, J.F., S.W. Squyres, R.E. Arvidson, H.M. Arneson, D. Bass, W. Calvin, W.H. Farrand, W. Goetz, M. Golombek, R. Greeley, J. Grotzinger, E. Guinness, A.G. Hayes, M.Y.H. Hubbard, K.E. Herkenhoff, M.J. Johnson, J.R. Johnson, J. Joseph, K.M. Kinch, M.T. Lemmon, R. Li, M.B. Madsen, J.N. Maki, M. Malin, E. McCartney, S. McLennan, H.Y. McSween, Jr., D.W. Ming, R.V. Morris, E.Z. Noe Dobrea, T.J. Parker, J. Proton, J.W. Rice, Jr., F. Seelos, J. Soderblom, L.A. Soderblom, J.N. Sohl-Dickstein, R.J. Sullivan, C. Weitz, M.J. Wolff (2004b) Pancam multispectral imaging results from the Opportunity rover at Meridiani Planum, *Science, 306,* 1703-1709.

526 Bell III, J.F., et al. (2008) Visible to near-IR multispectral orbital observations of Mars, Ch. 8, in
527 The Martian Surface: Composition, Mineralogy, and Physical Properties, Cambridge
528 University Press, p. 169-192.

529 Bell, J.F. III, A. Godber, M.S. Rice, A.A. Fraeman, B.L. Ehlmann, W. Goetz, C.J. Hardgrove,
530 D.E. Harker, J.R. Johnson, K.M. Kinch, M.T. Lemmon, S McNair, S. Le Mouélic, M.B.
531 Madsen, and the MSL Science Team (2013) Initial Multispectral Imaging Results from the
532 Mars Science Laboratory Mastcam Investigation at the Gale Crater Field Site, Lunar and
533 Planetary Science Conference, 44, abstract #1417.

534 Bell J.F. III, J.N. Maki, G.L. Mehall, M.A. Ravine M.A. Caplinger, and the Mastcam-Z Science
535 Team (2014) Mastcam-Z: A Geologic, Stereoscopic,and Multispectral Investigation on the
536 NASA Mars-2020 Rover, Abstract #1151, Presented at "International Workshop on
537 Instrumentation for Planetary Missions (IPM-2014)," Greenbelt, Maryland, November 4-7.

538 Bish, D., D. Blake, D. Vaniman, P. Sarrazin, T. Bristow, C. Achilles, P. Dera, S. Chipera, J.
539 Crisp, R.T. Downs, J. Farmer, M. Gailhanou, D. Ming, J.M. Morookian, R. Morris, S.
540 Morrison, E. Rampe, A. Treiman, and A. Yen (2014) The first X-ray diffraction
541 measurements on Mars, IUCrJ, 1(6), doi:10.1107/S2052252514021150.

542 Bishop, J. L., & Murad, E. (1996). Schwertmannite on Mars? Spectroscopic analyses of
543 schwertmannite, its relationship to other ferric minerals, and its possible presence in the
544 surface material on Mars. Mineral Spectroscopy: A Tribute to Roger G. Burns, 5, 337-358.

545 Bishop, Janice L., Enver Murad, and M. Darby Dyar. "What Lurks in the Martian Rocks and
546 Soil? Investigations of Sulfates, Phosphates, and Perchlorates. Akaganéite and
547 schwertmannite: Spectral properties and geochemical implications of their possible presence
548 on Mars." American Mineralogist 100, no. 4 (2015): 738-746.

549 Blake, D.F., et al. Curiosity at Gale Crater, Mars: Characterization and analysis of the Rocknest
550 sand shadow (2013) Science, 341(6153):1239505, doi:10.1126/science.1239505.

551 Blaney, D. L., et al. (2014) Chemistry and texture of the rocks at Rocknest, Gale Crater:
552 Evidence for sedimentary origin and diagenetic alteration, Journal of Geophysical Research
553 Planets, 119, doi:10.1002/ 2013JE004590.

554 Bridges, J.C., S.P. Schwenzer, R. Leveille, F. Westall, R.C. Wiens, N. Mangold, T. Bristow, P.
555 Edwards, and G. Berger (2015) Diagenesis and clay mineral formation at Gale Crater, Mars,
556 Journal of Geophysical Research Planets, 120(1):1-19, doi:10.1002/2014JE004757.

557 Bristow, T.F., D.L. Bish, D.T. Vaniman, R.V. Morris, D.F. Blake, J.P. Grotzinger, E.B. Rampe,
558 J.A. Crisp, C.N. Achilles, D.W. Ming, B.L. Ehlmann, P.L. King, J.C. Bridges, J.L.
559 Eigenbrode, D.Y. Sumner, S.J. Chipera, J.M. Morookian, A.H. Treiman, S.M. Morrison, R.T.
560 Downs, J.D. Farmer, D. Des Marais, P. Sarrazin, M.M. Floyd, M.A. Mischna, and A.C.

McAdam (2015) The origin and implications of clay minerals from Yellowknife Bay, Gale crater, Mars, American Mineralogist, 100(4):824-836, doi:10.2138/am-2015-5077.

Cavanagh, P.D. et al. (2015) Confidence Hills mineralogy and CheMin results from base of Mt. Sharp, Pahrump Hills, Gale Craer, Mars, Lunar and Planetary Science Conference abstract #2735.

Clark, R. N., et al (2003), USGS Digital Spectral Library splib05a, USGS Open File Report 03-395.

Clegg, S. M., Wiens, R. C., Maurice, S., Gasnault, O., Sharma, S. K., Misra, A. K., ... & Johnson, J. R. (2015). Remote Geochemical and Mineralogical Analysis with SuperCam for the Mars 2020 Rover. In Lunar and Planetary Science Conference (abstract #2781).

Cloutis, E.A., et al. (2006a) Detection and discrimination of sulfate minerals using reflectance spectroscopy, Icarus, 184, 121-157.

Cloutis, E.; Craig, M.; Kaletzke, L.; McCormack, K.; Stewart, L. (2006b) HOSERLab: A New Planetary Spectrophotometer Facility, 37th Annual Lunar and Planetary Science Conference, abstract no.2121.

Cloutis, E.S., M.A. Craig, R.V. Kruzeleck, W.R. Jamroz, A. Scott, F.C. Hawthorne, and S.A. Mertzman (2008) Spectral reflectance properties of minerals exposed to simulated Mars surface conditions, Icarus, 195, 140-169.

Cloutis, E.A., P. Hudon, T. Hiroi, M.J. Gaffey, and P. Mann (2011) Spectral reflectance properties of carbonaceous chondrites: 2. CM chondrites. Icarus 216, 309-346.

Cousin, A., P.Y. Meslin, R.C. Wiens, W. Rapin, N. Mangold, C. Fabre, O. Gasnault, O. Forni, R. Tokar, A. Ollila, S. Schröder, J. Lasue, S. Maurice, V. Sautter, H. Newsom, D. Vaniman, S. Le Mouélic, D. Dyar, G. Berger, D. Blaney, M. Nachon, G. Dromart, N. Lanza, B. Clark, S. Clegg, W. Goetz, J. Berger, B. Barraclough, D. Delapp, and MSL Science Team (2015) Compositions of coarse and fine particles in martian soils at Gale: A window into the production of soils, Icarus, 249:22-42, doi:10.1016/j.icarus.2014.04.052.

Dixon, E. M., A. S. Elwood Madden, E. M. Hausrath, and M. E. Elwood Madden (2015) Assessing hydrodynamic effects on jarosite dissolution rates, reaction products, and preservation on Mars, Journal of Geophysical Research Planets, 120, 625–642, doi:10.1002,2014JE004779.

Downs, R.T. and the MSL Science Team (2015) Determining mineralogy on Mars with the CheMin X-ray diffractometer, Elements, 11(1):45-50, doi:10.2113/gselements.11.1.45.

Ehlmann, B.L. and C.S. Edwards, (2014) Mineralogy of the martian surface, Annual Reviews of Earth and Planetary Sciences, 42:291-315, doi:10.1146/annurev-earth-060313-055024.

595 Ehlmann, B.L. and J. Buz (2015) Mineralogy and fluvial history of the watersheds of Gale,
596 Knobel, and Sharp craters: A regional context for MSL Curiosity's exploration, Geophysical
597 Research Letters, 42(2):264-273, doi:10.1002/2014GL062553.

598 Farrand, W., J.F. Bell III, J.R. Johnson, S.W. Squyres, J. Soderblom, and D.W. Ming (2006)
599 Spectral variability in Visible and Near Infrared multispectral Pancam data collected at Gusev
600 Crater: Examinations using spectral mixture analysis and related techniques, Journal of
601 Geophysical Research, 111, E02S15, doi:10.1029/2005JE002495.

602 Farrand, W. H.; et al. (2007) Visible and near-infrared multispectral analysis of rocks at
603 Meridiani Planum, Mars, by the Mars Exploration Rover Opportunity, Journal of Geophysical
604 Research, 112, E06S02, 10.1029/2006JE002773.

605 Farrand, W. H., J. F. Bell, III, J. R. Johnson, R. E. Arvidson, L. S. Crumpler, J. A. Hurowitz, and
606 C. Schröder (2008a) Rock spectral classes observed by the Spirit Rover's Pancam on the
607 Gusev Crater Plains and in the Columbia Hills, Journal of Geophysical Research, 113,
608 E12S38, doi:10.1029/2008JE003237.

609 Farrand, W.H., J. F. Bell III, J. R. Johnson, J.L. Bishop, R. V. Morris (2008b) Multispectral
610 Imaging from Mars Pathfinder, Ch. 8, *in The Martian Surface: Composition, Mineralogy,*
611 *and Physical Properties*, Cambridge University Press.

612 Fouchet, T., Montmessin, F., Forni, O., Maurice, S., Wiens, R. C., Jonhson, J. R., ... &
613 SuperCam Team, T. (2015). The Infrared Investigation on the SuperCam Instrument for the
614 Mars2020 Rover. In Lunar and Planetary Science Conference abstract #1736.

615 Fraeman, A. A., Arvidson, R. E., Catalano, J. G., Grotzinger, J. P., Morris, R. V., Murchie, S. L.,
616 ... & Viviano, C. E. (2013) A hematite-bearing layer in Gale Crater, Mars: Mapping and
617 implications for past aqueous conditions. Geology, 41(10), 1103-1106.

618 Fraeman, A. A. C. S. Edwards, B. L. Ehlmann, R. E. Arvidson, J. R. Johnson, and M.S. Rice
619 (2015) Exploring Curiosity's Future Path From Orbit: The View Of Lower Mt. Sharp From
620 Integrated CRISM, HiRise, and THEMIS Datasets, Lunar and Planetary Science Conference,
621 abstract # 2124.

622 Grotzinger, J. P., & Milliken, R. E. (2012). The sedimentary rock record of Mars: Distribution,
623 origins, and global stratigraphy. In Sedimentary Geology of Mars (Vol. 102, pp. 1-48). SEPM
624 Special Publication, Tulsa, OK.

625 Grotzinger, J.P., et al. (2014) A habitable fluvio-lacustrine environment at Yellowknife Bay,
626 Gale Crater, Mars, Science, 343(6169), 1242777, doi:10.1126/science.1242777.

627 Grotzinger, J.P., J.A. Crisp, A.R. Vasavada, and the MSL Science Team (2015a) Curiosity's
628 mission of exploration at Gale Crater, Mars, Elements, 11(1):19-26,
629 doi:10.2113/gselements.11.1.19.

630 Grotzinger, J.P., et al. (2015b) Deposition,Exhumation, and Paleoclimate of an Ancient Lake
631 Deposit, Gale Crater, Mars (in review).

632 Jackson, R.S., R.C. Wiens, D.T. Vaniman, L. Beegle, O. Gasnault, H.E. Newsom, S. Maurice,
633 P.-Y. Meslin, S. Clegg, A. Cousin, S. Schröder, J.M. Williams (2015) ChemCam
634 Investigation of the John Klein and Cumberland Drill Holes and Tailings, submitted to Icarus.

635 Johnson, J.R. and Grundy, W.M. (2001) Visible/near-infrared spectra and two-layer modeling of
636 palagonite-coated basalts. Geophysical Research Letters, 28, 2101-2104.

637 Johnson, J.R., and 10 others (2001) Geological characterization of remote field sites using visible
638 and infrared spectroscopy: Results from the 1999 Marsokhod field test, Journal of
639 Geophysical Research, 106, 7683-7711.

640 Johnson, J.R., W.M. Grundy, and M.T. Lemmon, (2003) Dust deposition at the Mars Pathfinder
641 landing site: Observations and modeling of visible/near-infrared spectra, Icarus, 163, 330-
642 346.

643 Johnson, J. R., J. F. Bell, III, E. Cloutis, M. Staid, W. H. Farrand, T. McCoy, M. Rice, A. Wang,
644 and A. Yen (2007) Mineralogic constraints on sulfur-rich soils from Pancam spectra at Gusev
645 crater, Mars, Geophysical Research Letters, 34, L13202, doi:10.1029/2007GL02989.

646 Johnson, J.R., J.F. Bell III , S. Bender , D. Blaney , E. Cloutis , L. DeFlores , B. Ehlmann, O.
647 Gasnault , B. Gondet , K. Kinch , M. Lemmon, S. Le Mouélic , S. Maurice , M. Rice, R.
648 Wiens, MSL Science Team (2015) ChemCam Passive Reflectance Spectroscopy of Surface
649 Materials at the Curiosity Landing Site, Mars, Icarus, 249, 74–92.

650 Lanza, N.L., A.M. Ollila, A. Cousin, R.C. Wiens, S. Clegg, N. Mangold, N. Bridges, D. Cooper,
651 M. Schmidt, J. Berger, R. Arvidson, N. Melikechi, H. E. Newsom, R. Tokar, C. Hardgrove,
652 A. Mezzacappa, R.S. Jackson, B. Clark, O. Forni, S. Maurice, M. Nachon, R.B. Anderson, J.
653 Blank, M. Deans, D. Delapp, R. Léveillé, R. McInroy, R. Martinez, P.-Y. Meslin, and P. Pinet
654 (2015) Understanding the signature of rock coatings in laser-induced breakdown spectroscopy
655 data, Icarus, 249:62-73, doi:10.1016/j.icarus.2014.05.038.

656 Lapotre, M. G. A., Ehlmann, B. L., Ayoub, F., Minson, S. E., Bridges, N. T., Fraeman, A. A., ...
657 & Johnson, J. R. (2015). The Bagnold Dunes at Gale Crater---A Key to Reading the Geologic
658 Record of Mount Sharp. In Lunar and Planetary Science Conference abstract #1634.

659 Lemmon, M.T., et al. (2004) Atmospheric imaging results from the Mars Exploration Rovers:
660 Spirit and Opportunity, Science, 306, 1753-1756.

661 Mangold, N., et al. (2015) Chemical variations in Yellowknife Bay formation sedimentary rocks
662 analyzed by ChemCam on board the Curiosity rover on Mars, Journal of Geophysical
663 Research Planets, 120(3):452-482, doi:10.1002/2014JE004681.

664 Maurice, S., et al. (2012), The ChemCam instrument suite on the Mars Science Laboratory
665 (MSL) rover: Science objectives and mast unit description, Space Sci. Rev., 170, 95–166,
666 doi:10.1007/s11214-012-9912-2.

667 McLennan, S.M., et al. (2014) Elemental geochemistry of sedimentary rocks at Yellowknife
668 Bay, Gale Crater, Mars, Science, 343(6169), 1244734, doi:10.1126/science.1244734.

669 McLennan, S. M., Dehouck, E., Grotzinger, J. P., Hurowitz, J. A., Mangold, N., & Siebach, K.
670 (2015). Geochemical Record of Open-System Chemical Weathering at Gale Crater and
671 Implications for Paleoclimates on Mars. In Lunar and Planetary Science Conference, abstract
672 # 2533.

673 McCollom, Thomas M., Bethany L. Ehlmann, Alian Wang, Brian M. Hynek, and Thelma S.
674 Berquó [2014] Detection of iron substitution in natroalunite-natrojarosite solid solutions and
675 potential implications for Mars, American Mineralogist 99, no. 5-6, 948-964.

676 McSween, H.Y., Jr., S.L. Murchie, J.A. Crisp, N.T. Bridges, R.C. Anderson, J.F. Bell III, D.T.
677 Britt, J. Brückner, G. Dreibus, T. Economou, A. Ghosh, M.Golombek, J.Greenwood, J.R.
678 Johnson, H.J. Moore, R.V. Morris, T. J. Parker, R. Singer, and H. Wänke (1999) Chemical,
679 multispectral, and textural constraints on the composition and origin of rocks at the Mars
680 Pathfinder landing site, Journal of Geophysical Research, 104, 8679-8715.

681 Milliken, R. E., J. P. Grotzinger, and B. J. Thomson, Paleoclimate of Mars as captured by the
682 stratigraphic record in Gale Crater (2010) Geophysical Research Letters 37, 4, DOI:
683 10.1029/2009GL041870.

684 Milton, E.J., et al. (2009) Progress in field spectroscopy, Rem. Sens. Environ., 113, S92-S109.

685 Morris, R. V., H. V. Lauer Jr., C. A. Lawson, E. K. Gibson Jr., G. A. Nace, and C. Stewart
686 (1985), Spectral and other physicochemical properties of submicron powders of hematite (α-
687 Fe2O3), maghemite (γ-Fe2O3), magnetite (Fe3O4), goethite (α-FeOOH), and lepidocrocite
688 (γ-FeOOH), J. Geophys. Res., 90(B4), 3126–3144, doi:10.1029/JB090iB04p03126.

689 Morris, R.V., D.C. Golden, J.F. Bell III, (1997) Low-temperature reflectivity spectra of red
690 hematite and the color of Mars, Journal of Geophysical Research, 102, 912-9133.

691 Morris, R. V., et al. (2000), Mineralogy, composition, and alteration of Mars Pathfinder rocks
692 and soils: Evidence from multispectral, elemental, and magnetic data on terrestrial analogue,
693 SNC meteorite, and Pathfinder samples, J. Geophys. Res., 105, 1757–1817,
694 doi:10.1029/1999JE001059.

695 Nachon, M., Clegg, S. M., Mangold, N., Schröder, S., Kah, L. C., Dromart, G., ... & Wellington,
696 D., Calcium sulfate veins characterized by ChemCam/Curiosity at Gale Crater, Mars (2014)
697 Journal of Geophysical Research: Planets, 119, doi:10.1002/2013JE004588.

698 Pitman, K.M., et al. (2014) Reflectance spectroscopy and optical functions for hydrated Fe-
699 sulfates, American Mineralogist, 99, 1593-1603.

700 Rampe, E.B., et al. (2015a), Potential cement phases in sedimentary rocks drilled by Curiosity at
701 Gale Crater, Mars, Lunar and Planetary Science Conference 46, abstract #2038.

702 Rampe, E. B., Ming, D. W., Blake, D. F., Vaniman, D. T., Chipera, S. J., Bish, D. L., Bristow, T.
703 F., Morris, R. V., Achilles, C. N., Cavanagh, P. D., Downs, R. T., Dyar, M. D., Fairen, A. G.,
704 Farmer, J. D., Franz, H. B., Fendrich, K. V., Grotzinger, J. P., Morrison, S. M., Morookian, J.
705 M., Sarrazin, P., Sumner, D. Y., Treiman, A. H., and Yen, A. S. (2015b) Curiosity's Pahrump
706 Hills campaign in Gale crater, Mars: Mineralogy of the sediments and evidence for post-
707 depositional acid-sulfate alteration (in preparation).

708 Rice, M. S., Bell III, J. F., Godber, A., Wellington, D., Fraeman, A. A., Johnson, J. R., ... &
709 Grotzinger, J. P. (2013) Mastcam multispectral imaging results from the Mars Science
710 Laboratory investigation in Yellowknife Bay. In European Planetary Science Congress 2013,
711 id. EPSC2013-762 (Vol. 8, p. 762).

712 Roush, T.L., D.L. Blaney, and R.B. Singer (1993) The surface composition of Mars as inferred
713 from spectroscopic observations. In Remote Geochemical Analysis: Elemental and
714 Mineralogical Composition, ed. C.M. Pieters and P.A.J. Englert, New York: Cambridge
715 University Press, pp. 367-393.

716 Rossman, G.R. (1975)Spectroscopic and magnetic studies of ferric iron hydroxyl sulfates:
717 Intensification of color in ferric iron clusters bridged by a single hydroxide ion, Amer.
718 Mineral. 60, 698-704.

719 Sautter, V., C. Fabre, O. Forni, M.J. Toplis, A. Cousin, A.M. Ollila, P.Y. Meslin, S. Maurice,
720 R.C. Wiens, D. Baratoux, N. Mangold, S. Le Mouélic, O. Gasnault, G. Berger, J. Lasue, R.A.
721 Anderson, E. Lewin, M. Schmidt, D. Dyar, B.L. Ehlmann, J. Bridges, B. Clark, and P. Pinet,
722 Igneous mineralogy at Bradbury Rise: The first ChemCam campaign at Gale crater (2014)
723 Journal of Geophysical Research Planets, 119(1): 30-46, doi:10.1002/2013JE004472.

724 Schmidt, M. E., P. L. King, R. Gellert, B. Elliott, L. Thompson, J. A. Berger, J. Bridges et al.
725 Geochemical diversity and K-rich compositions found by the MSL APXS in Gale Crater,
726 Mars (2013), Mineralogical Magazine 77, no. 5, 2158.

727 Schmidt, M.E., J.L. Campbell, R. Gellert, G.M. Perrett, A.H. Treiman, D.L. Blaney, A. Ollila,
728 F.J. Calef III, L. Edgar, B.E. Elliott, J. Grotzinger, J. Hurowitz, P.L. King, M.E. Minitti, V.
729 Sautter, K. Stack, J.A. Berger, J.C. Bridges, B.L. Ehlmann, O. Forni, L.A. Leshin, K.W.

730 Lewis, S.M. McLennan, D.W. Ming, H. Newsom, I. Pradler, S.W. Squyres, E.M. Stolper, L.
731 Thompson, S. VanBommel, and R.C. Wiens (2014) Geochemical diversity in first rocks
732 examined by the Curiosity rover in Gale crater: Evidence for and significance of an alkali and
733 volatile-rich igneous source, Journal of Geophysical Research Planets, 119(1):64-81,
734 doi:10.1002/2013JE004481.

735 Seelos, K. D., Seelos, F. P., Viviano-Beck, C. E., Murchie, S. L., Arvidson, R. E., Ehlmann, B.
736 L., & Fraeman, A. A. (2014). Mineralogy of the MSL Curiosity landing site in Gale crater as
737 observed by MRO/CRISM. Geophysical Research Letters, 41(14), 4880-4887.

738 Sherman, D. M., R. G. Burns, and V. M. Burns (1982), Spectral characteristics of the iron oxides
739 with application to the Martian bright region mineralogy, J. Geophys. Res., 87(B12), 10169–
740 10180, doi:10.1029/JB087iB12p10169.

741 Singer, R.B., T. B. McCord, R. N. Clark, J.B. Adams, and R.L. Huguenin (1979) Mars surface
742 composition from reflectance spectroscopy: A summary, Journal of Geophysical Research,
743 84, 8415-8426.

744 Skulte, E.C., H.B. Jensen, A.D. Rogers, and R. J. Reeder (2015) Morphological, structural, and
745 spectral characteristics of amorphous iron sulfates, Journal of Geophysical Research Planets,
746 120, doi:10.1002/2014JE004784.

747 Sobron, P., J.L. Bishop, D.F. Blake, B. Chen, and F. Rull (2014), Natural Fe-bearing oxides and
748 sulfates from the Rio Tinto Mars analog site: Critical assessment of VNIR reflectance
749 spectroscopy, laser Raman spectroscopy, and XRD as mineral identification tools, Amer.
750 Mineral. 99, 1199-1205.

751 Stack, K. M., Grotzinger, J. P., Gupta, S., Kah, L. C., Lewis, K. W., McBride, M. J., ... & Yingst,
752 R. A. (2015). Sedimentology and Stratigraphy of the Pahrump Hills Outcrop, Lower Mount
753 Sharp, Gale Crater, Mars. In Lunar and Planetary Science Conference, abstract #1994.

754 Stolper, E.M., M.B. Baker, M.E. Newcombe, M.E. Schmidt, A.H. Treiman, A. Cousin, M.D.
755 Dyar, M.R. Fisk, R. Gellert, P.L. King, L. Leshin, S. Maurice, S.M. McLennan, M.E. Minitti,
756 G. Perrett, S. Rowland, V. Sautter, R.C. Wiens, and MSL Science Team (2013) The
757 petrochemistry of Jake_M: A martian mugearite, Science, 341 (6153):1239463,
758 doi:10.1126/science.1239463.

759 Thompson, L. et al. (2015) The composition of the Basal Murray Formation at Pahrump Hills,
760 Gale crater, Mars: implications for provenance and alteration history from an APXS
761 perspective, in preparation.

762 Treiman, A.H., R.V. Morris, D.G. Agresti, T.G. Graff, C.N. Achilles, E.B. Rampe, T.F. Bristow,
763 D.W. Ming, D.F. Blake, D.T. Vaniman, D.L. Bish, S.J. Chipera, S.M. Morrison, and R.T.

764 Downs (2014) Ferrian saponite from the Santa Monica Mountains (California, U.S.A., Earth):
765 Characterization as an analog for clay minerals on Mars with application to Yellowknife Bay
766 in Gale Crater, American Mineralogist, 99, doi:10.2138/am-2014-4763, 2234-2250.

767 Treiman, A.H. et al. (2015a) Mineralogy and genesis of the Windjana sandstone, Kimberley
768 area, Gale Crater, Mars, Lunar and Planetary Science Conference 46, abstract #2620.

769 Treiman, A.H. et al. (in preparation), Mineralogy and genesis of the Windjana sandstone,
770 (Kimberley area, Gale Crater, Mars) by CheMin X-ray diffraction: Sediment components, and
771 the nature of potassic rocks and sediments in Gale Crater, in preparation to Journal of
772 Geophysical Research, 2015b.

773 Vaniman, D.T., et al. (2014) Mineralogy of a mudstone at Yellowknife Bay, Gale Crater, Mars,
774 Science, 343(6169), 1243480, doi:10.1126/science.1243480.

775 Vasavada, A.R., J.P. Grotzinger, R.E. Arvidson, F.J. Calef, J.A. Crisp, S. Gupta, J. Hurowitz, N.
776 Mangold, S. Maurice, M.E. Schmidt, R.C. Wiens, R.M.E. Williams, and R.A. Yingst (2014)
777 Overview of the Mars Science Laboratory mission: Bradbury landing to Yellowknife Bay and
778 beyond, Journal of Geophysical Research Planets, 119(6):1134-1161,
779 doi:10.1002/2014JE004622.

780 Wellington, D., et al. (2014) Visible to Near-IR Spectral Units along the MSL Gale Crater
781 Traverse: Comparison of In Situ Mastcam and Orbital CRISM Observations, AGU Fall
782 Meeting, P43D-4015.

783 Wellington, D., J. Bell, J. Johnson, K. Kinch., M. Rice, A. Fraeman (this issue) Visible and
784 Near-Infrared Spectra of Select High-Interest Science Targets within Gale Crater Observed by
785 MSL Mastcam.

786 Wiens, R. and 80 others (2012) The ChemCam Instrument Suite on the Mars Science Laboratory
787 (MSL) Rover: Body Unit and Combined System Performance, Space Sci Rev., 170, 167-227.

788 Wiens, R. C., et al. (2013) Pre-flight calibration and initial data processing for the ChemCam
789 laser-induced breakdown spectroscopy instrument on the Mars Science Laboratory rover,
790 Spectrochimica Acta Part B: Atomic Spectroscopy 82, 1-27.

791 Wiens, R.C., S. Maurice, and the MSL Science Team (2015) ChemCam: Chemostratigraphy by
792 the first Mars microprobe, Elements, 11(1):33-38, doi:10.2113/gselements.11.1.33.

793 Williams, R.M.E., et al. (2013) Martian fluvial conglomerates at Gale Crater, Science,
794 340(6136):1068-1072, doi:10.1126/science.1237317.

795 Wray, J.J., (2013) Gale crater: The Mars Science Laboratory/Curiosity rover landing site,
796 International Journal of Astrobiology, 12(1):25-38, doi:10.1017/S1473550412000328.

797

Table 1. ChemCam observations used in this study.

Target	Sol	Sequence ID	Exposure time (msec)	LTST	Phase angle *(deg)*	τ_{880}[1]
Cumberland 2	289	2289	3	13:26	43	0.98
Windjana	619	2619	3	13:33	84	0.34
Perdido2	728	1728	30	11:41	22	0.76
Bonanza King	728	2728	30	11:48	27	0.76
Confidence Hills (Stovepipe Wells)	762	2762	3	13:06	41	0.88
Mojave_1	869	3869	30	12:04	49	0.92
Telegraph Peak	910	1910	30	10:29	58	0.80
Dunes	432	3432	30	11:27	80	0.64
Hematite Ridge 1	467	2466	30	12:00	68	0.44
Hematite Ridge 2	467	3466	30	12:15	68	0.44
Hematite Ridge 3	475	1475	30	12:51	70	0.45
Hematite Ridge 4	475	2475	30	13:07	72	0.45
Hematite Ridge 5	492	1492	30	11:20	64	0.46
Hematite Ridge 6	492	2492	30	11:35	65	0.46

[1]interpolated from preliminary atmospheric opacity measurements acquired at 880 nm

Table 2. Summary of CheMin results for drilled samples for minerals of interest.

Target	Jarosite (wt%)	Hematite (wt%)	Magnetite (wt%)
Cumberland 2	0	1	4
Windjana	<1?	1	12
Confidence Hills (Stovepipe Wells)	1.1	8.4	3.8
Mojave_1	3.5	3.1	3.5
Telegraph Peak	1.5	1.3	8.7

Table 3. 433 nm band depths of drill tailing spectra.

Target	Sol	Sequence ID	Raster location #	Exposure time (msec)	433 nm band depth
Cumberland 2	289	2289	1	3	0.023
Windjana	619	2619	1	3	0.047
Perdido2	728	1728	5	30	0.071
Bonanza King	728	2728	2	30	0.018
Confidence Hills (Stovepipe Wells)	762	2762	10	3	0.035
Mojave_1	869	3869	3	30	0.028
Telegraph Peak	910	1910	3	30	0.018

433 nm band depth computed using continuum calculated between 415 nm and 460 nm wavelengths (±5 nm averaging used).

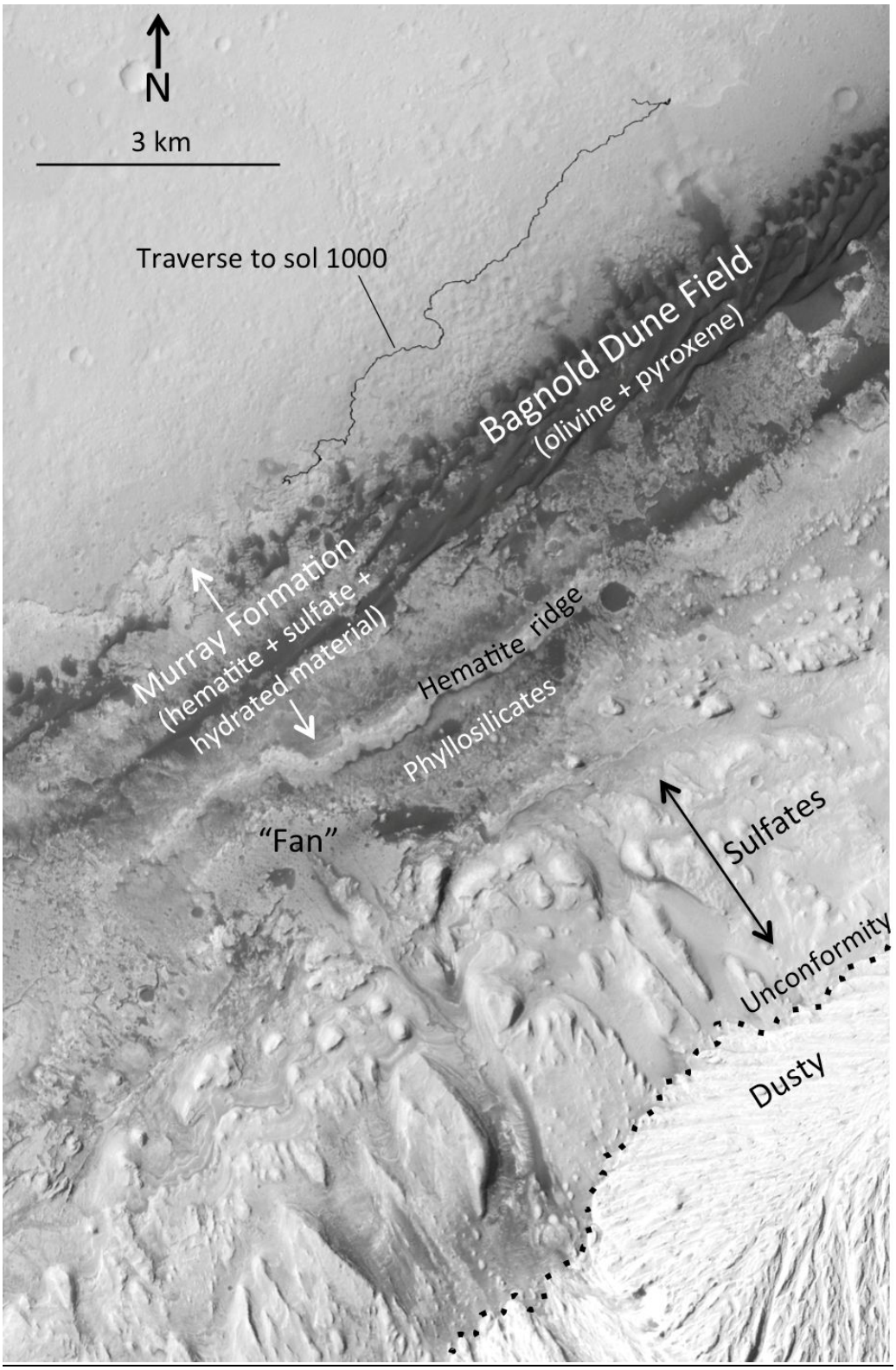

806

807 **Figure 1a.** Generalized orbital mineralogical map and Curiosity traverse path through Sol 1000
808 showing location of Hematite Ridge and nearby regions of interest. Based on mapping and data
809 from Milliken et al. (2010), Anderson and Bell (2010), and Fraeman et al. (2013).

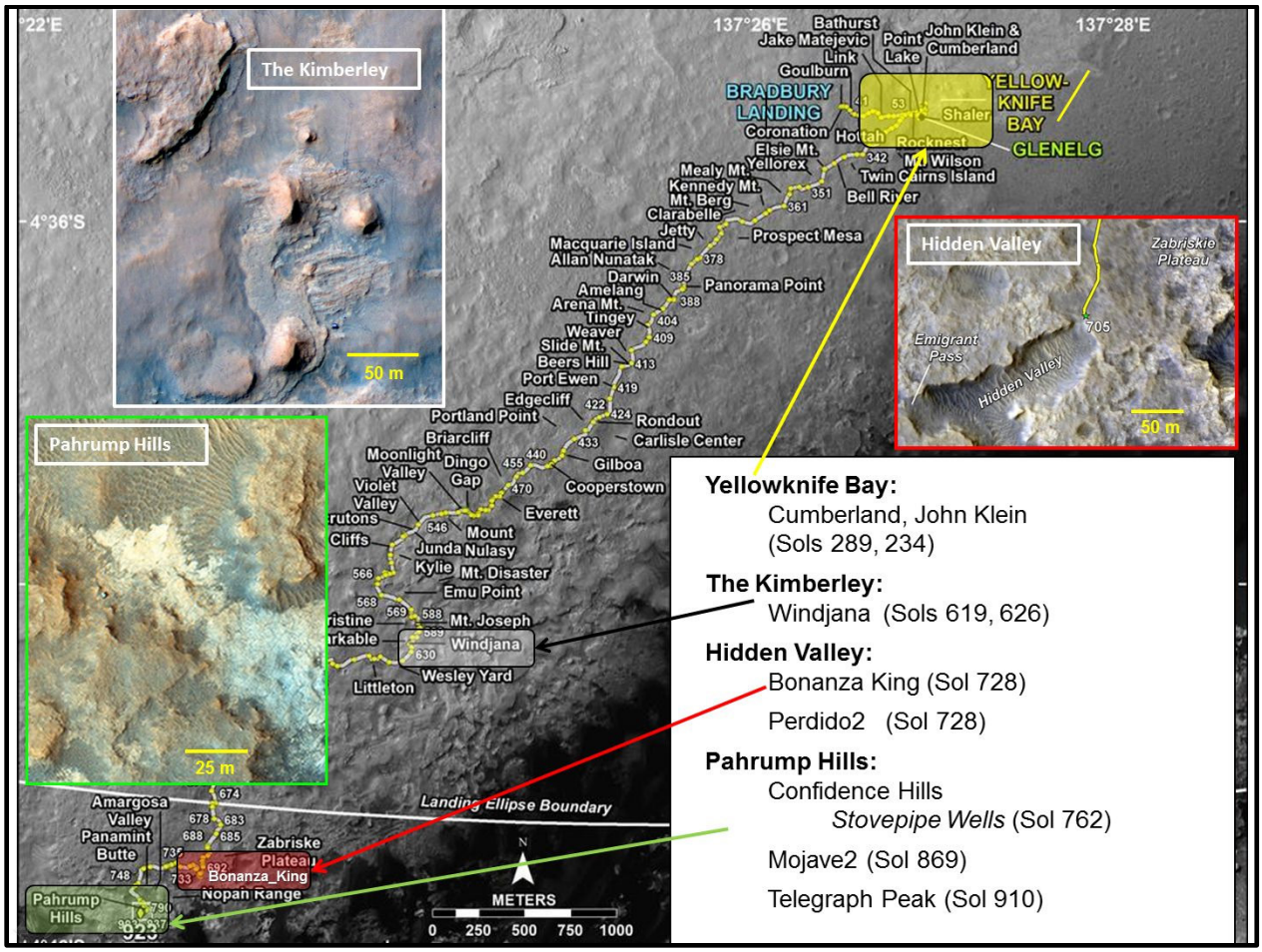

Figure 1b. Curiosity traverse map with areas of interest shown, along with inset false-color HiRISE images showing views of Hidden Valley, The Kimberley, and Pahrump Hills regions. (Base map from mars.nasa.gov/msl/multimedia/images/?ImageID=6993).

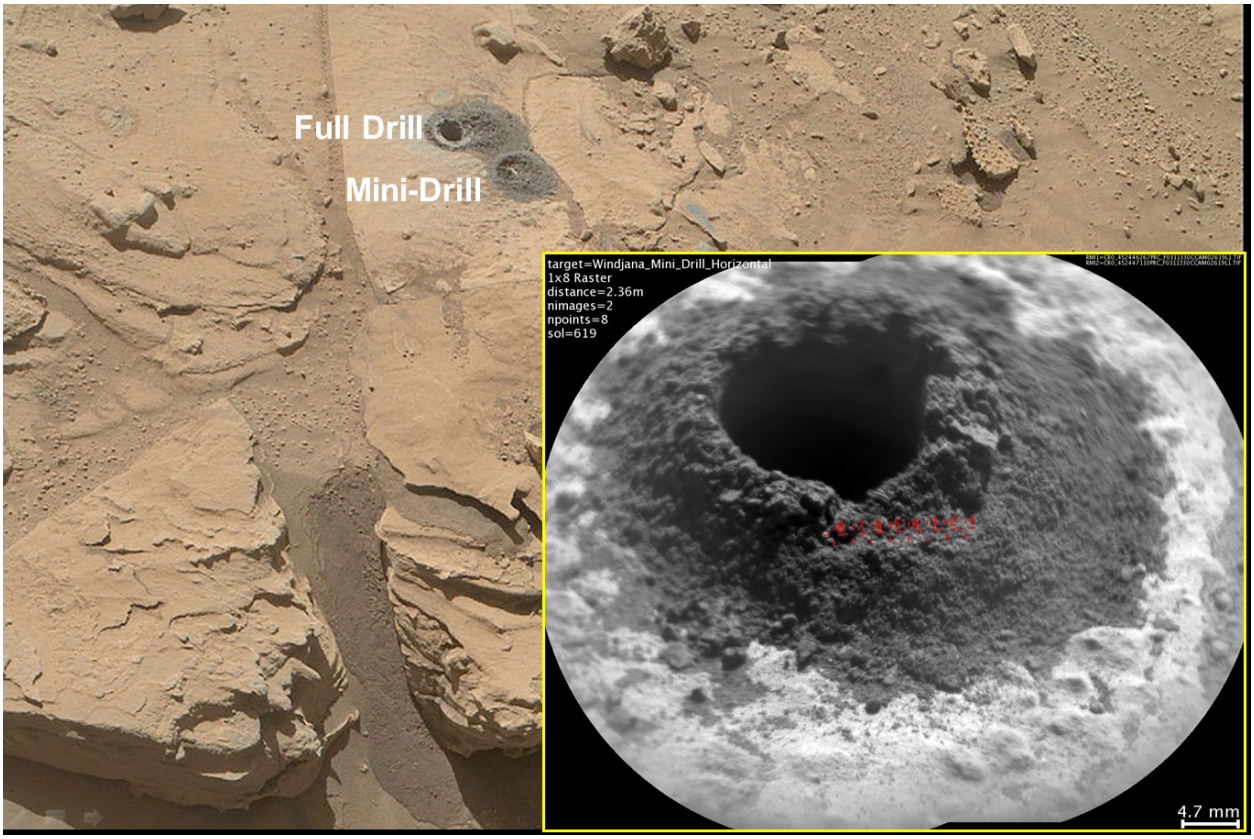

Figure 2. Sol 626 Mastcam M-34 image (0626ML0026760010302385E01) showing Windjana mini-drill and full drill locations, along with Sol 619 RMI mosaic of mini-drill hole and tailings (ccam02619; CR0_452446267, CR0_452447110) showing raster of eight locations.

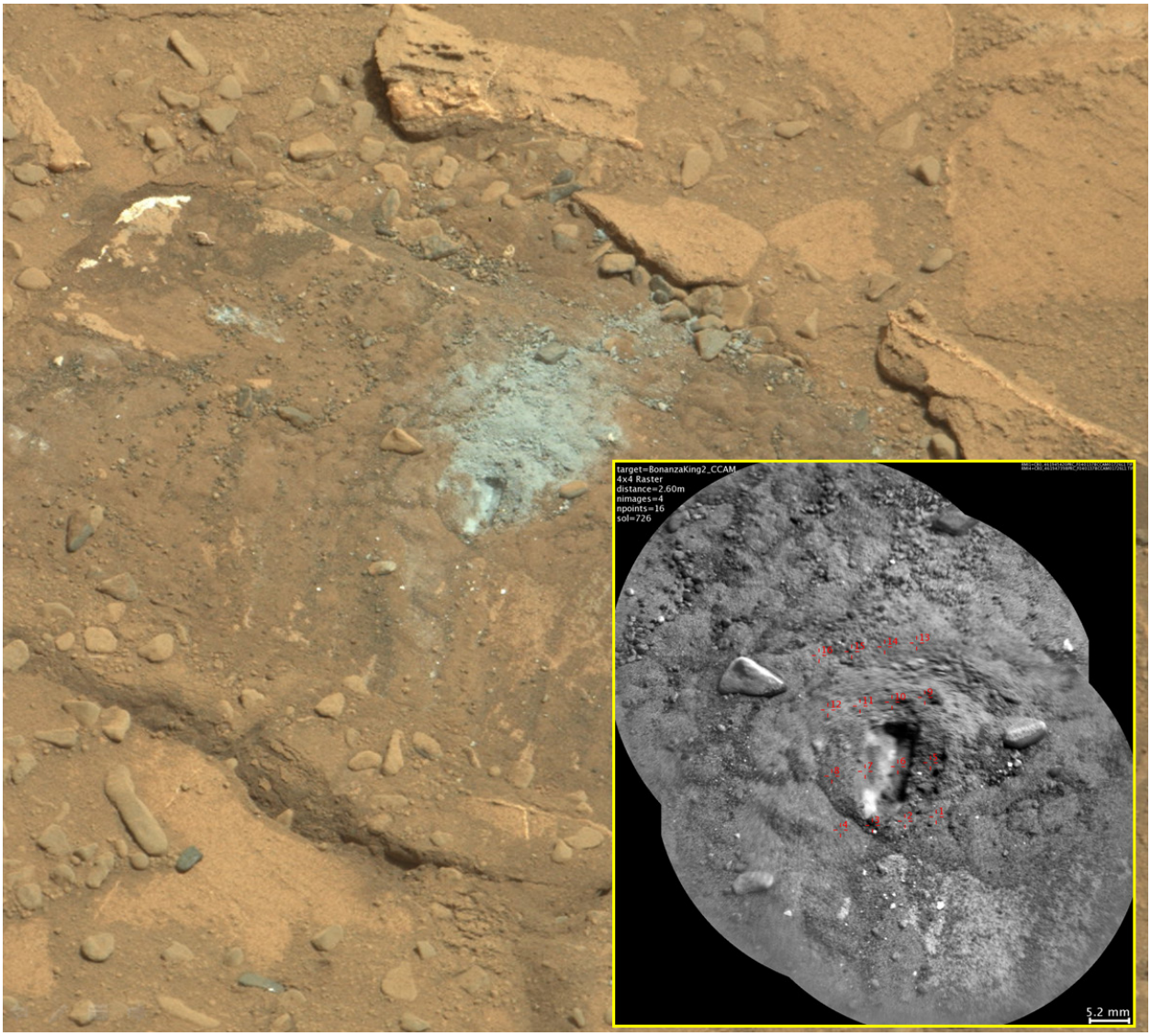

Figure 3. Portion of Sol 726 Mastcam M-100 image (0726MR0031010010402920E01) showing Bonanza_King target after attempted mini-drill activities, along with Sol 726 RMI mosaic of partial mini-drill area (ccam01726; CR0_461945420, CR0_461947398) and 4x4 ChemCam raster locations.

Figure 4. Portion of Sol 725 Mastcam M-100 image (0725MR0030940000402844E01) showing Perdido2 target, along with Sol 728 RMI mosaic (ccam01728; CR0_462114621, CR0_462115029) showing 5x1 ChemCam passive raster locations. This was acquired after a ChemCam LIBS observation on Sol 725 (sequence 3725) on the broken rock Perdido (directly above this raster) exhibited passive spectra (3 msec "dark" exposures) with a potential 433 nm absorption band.

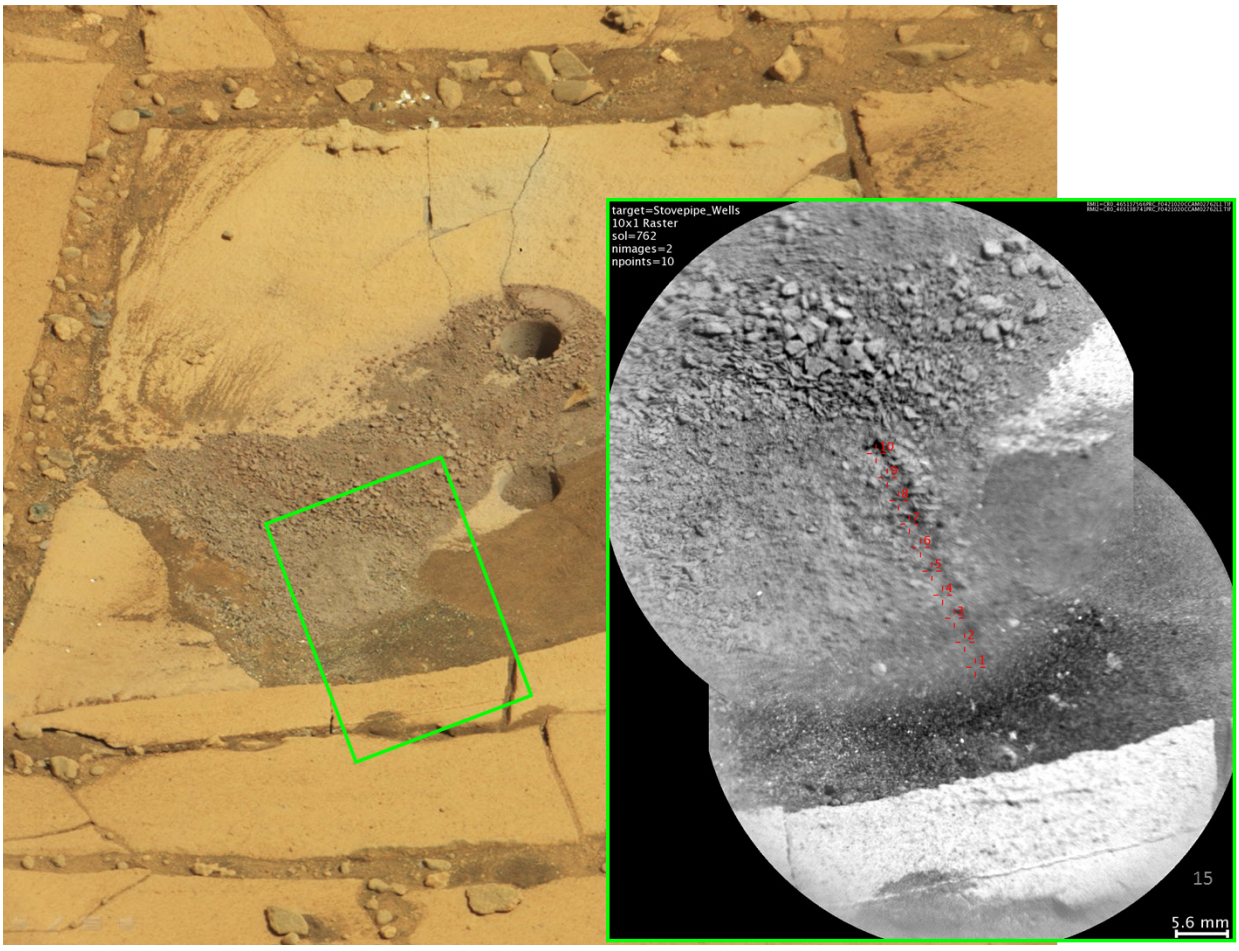

Figure 5. Sol 759 Mastcam M-100 image (0759MR0032680010403804E01) showing Stovepipe Wells target (green box) and the Confidence Hills mini-drill and full drill holes, along with Sol 762 RMI mosaic (ccam02762; CR0_465137566, CR0_465138741) showing 10x1 ChemCam raster locations on Stovepipe Wells (locations #4-10 occur on drill tailings).

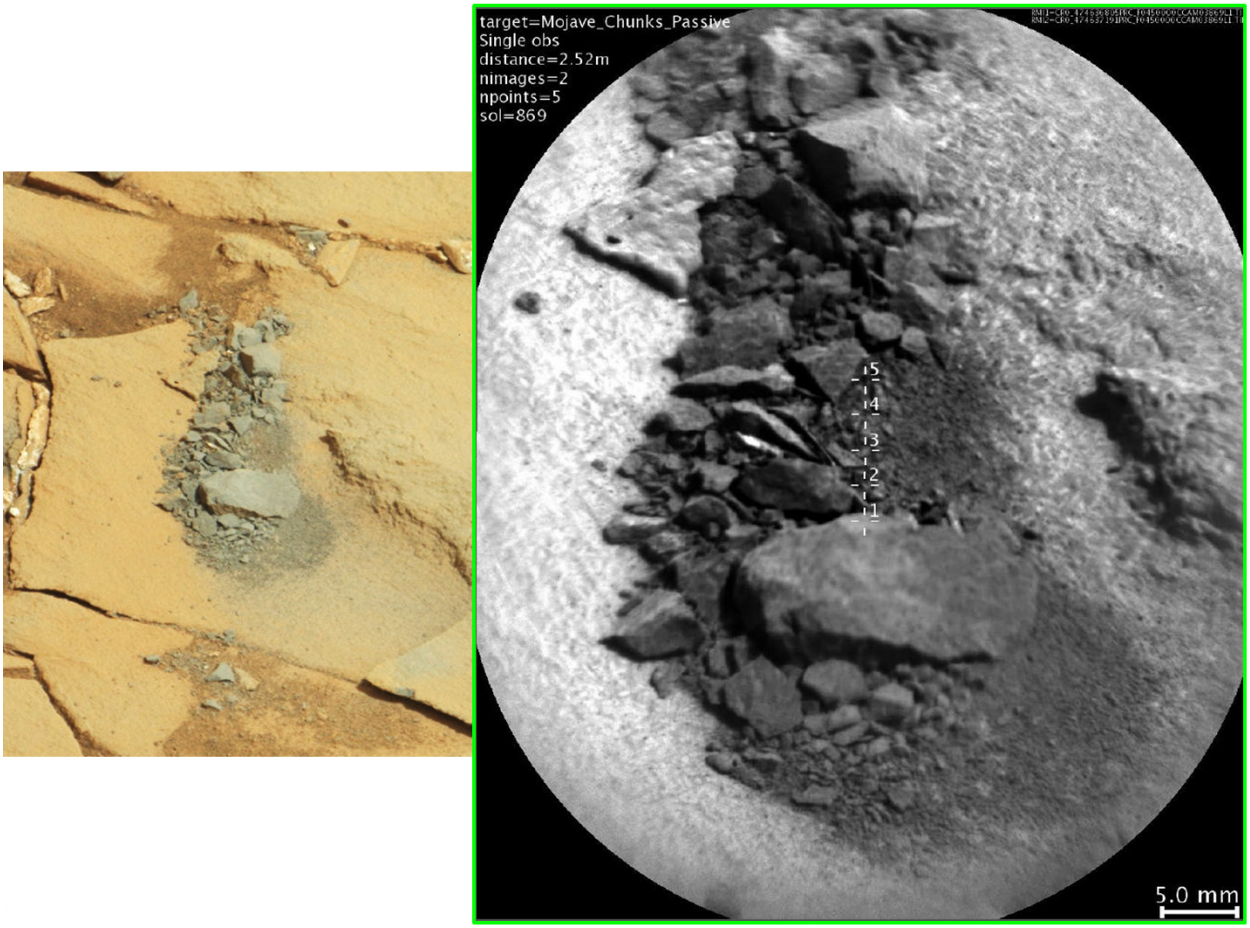

Figure 6. Portion of Sol 868 Mastcam M-100 image (0868MR0038120020501122E01) showing fragments generated by mini-drill attempt on target Mojave_1, along with Sol 869 RMI mosaic (ccam03869; CR0_474636805, CR0_474637191) showing 1x5 ChemCam passive raster locations.

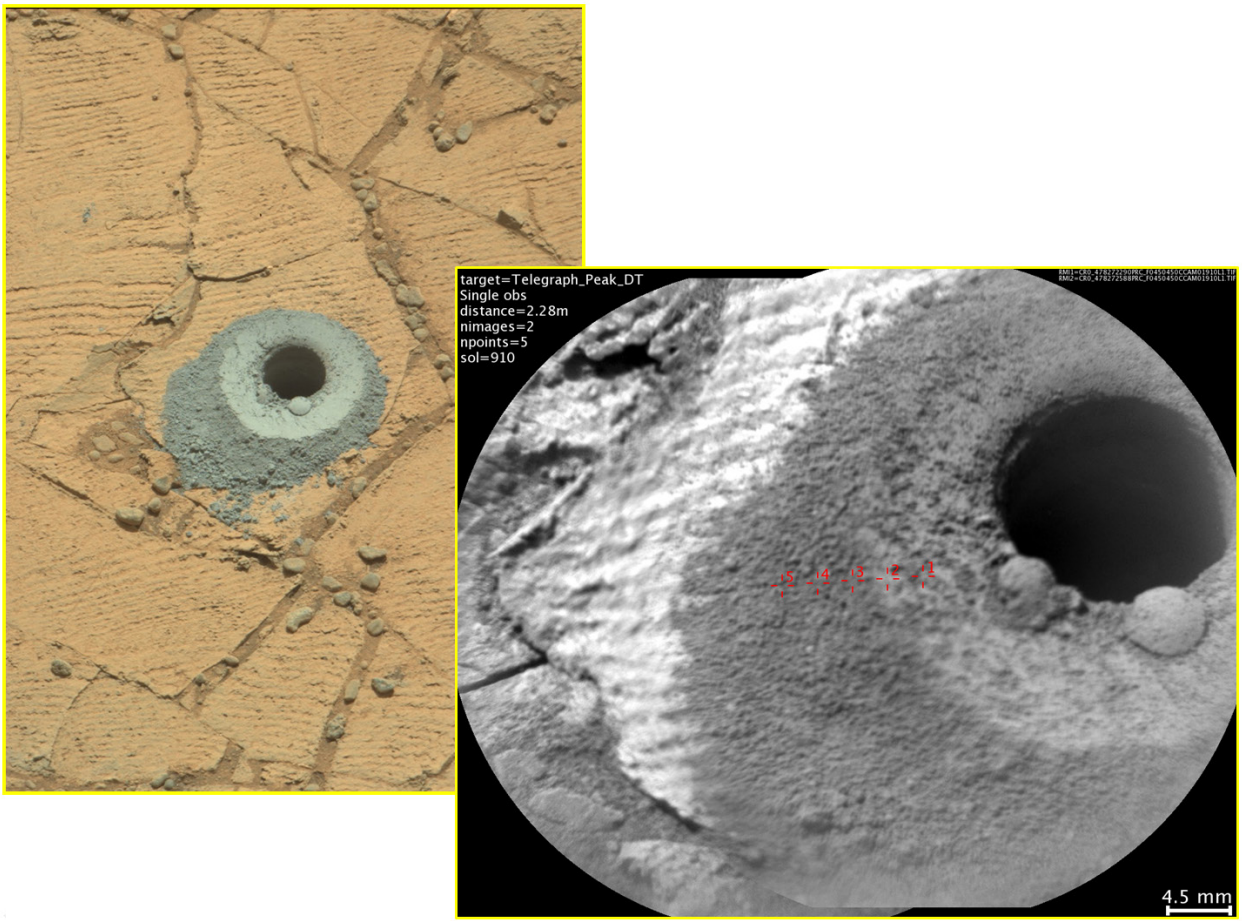

840

841 **Figure 7.** Portion of Sol 908 Mastcam M-100 image (0908MR0039720010501423E01) showing
842 full drill hole on Telegraph Peak target, along with Sol 910 RMI mosaic (ccam01910;
843 CR0_478272290, CR0_478272588) showing 5x1 ChemCam passive raster locations.

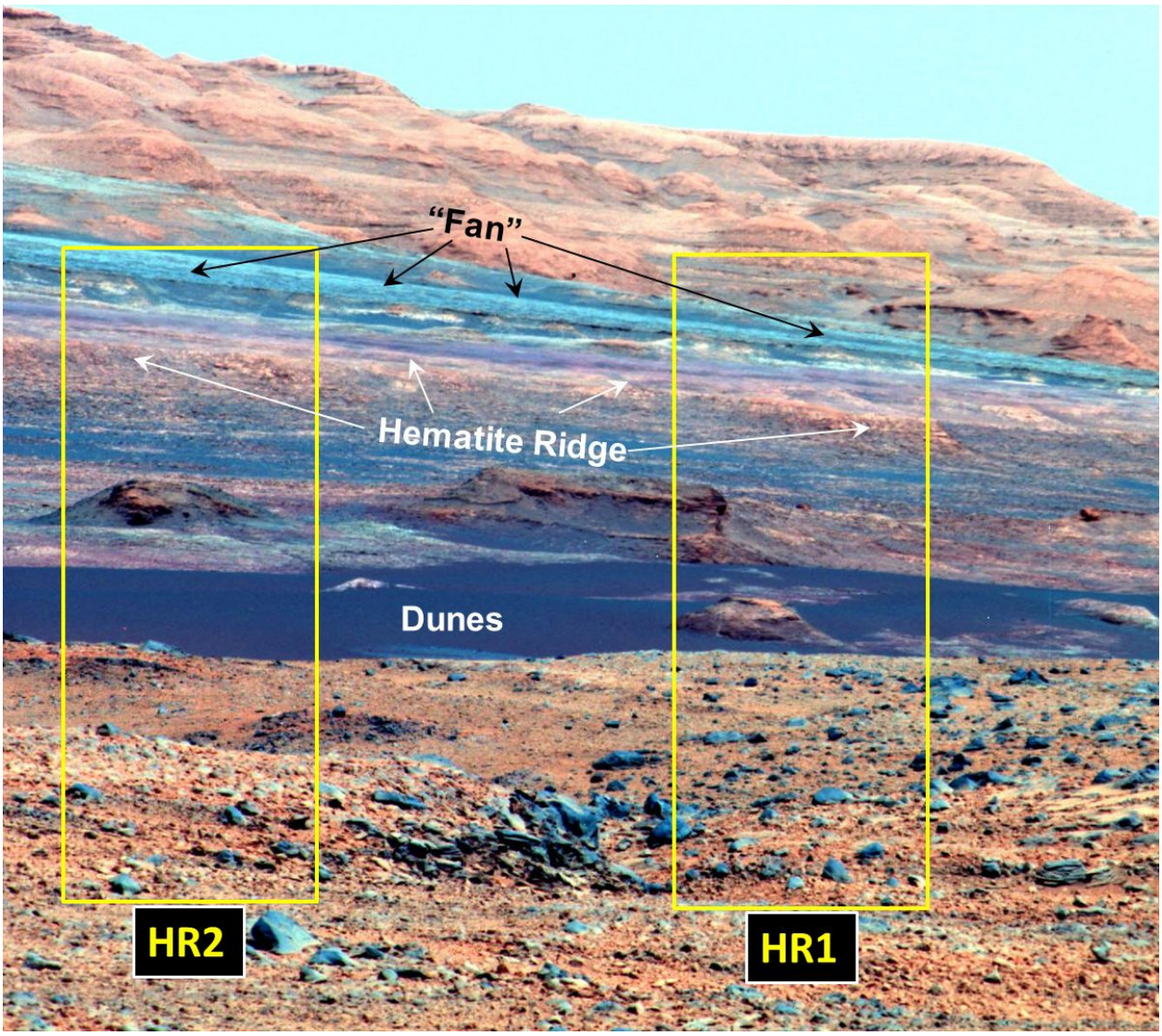

Figure 8. Portion of Sol 468 M-100 false-color image (sequence mcam01864; red = 805 nm, green = 527 nm, blue = 447 nm) view toward 195° azimuth. Portion of Bagnold Dunes shown along with Hematite Ridge promontory, and "fan" materials near base of Mt. Sharp (cf. Fig. 1a). Superimposed are outlines of HR1 and HR2 RMI mosaics acquired on Sol 467 (Figure 14a-b).

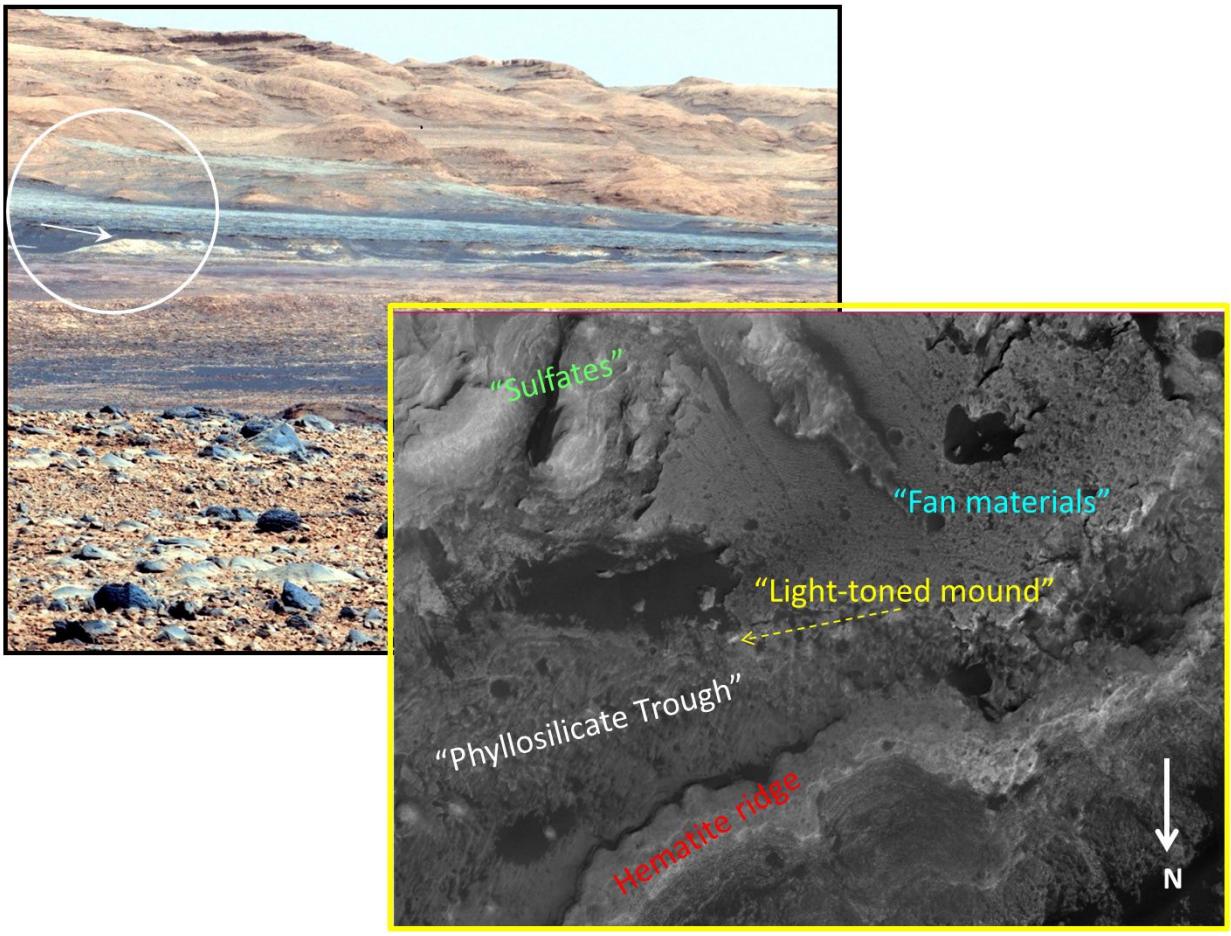

Figure 9. (*top*) Portion of Sol 475 Mastcam M-100 enhanced image 0475MR0018870000302889E01 (RGB=751, 527, 445 nm) showing light-toned mound (white arrow within white circle) featured in Figure 15; (*bottom*); HiRISE image (with North at bottom to facilitate comparison with rover's perspective looking south) labeled with general mapped units (cf. Figure 1). "Light-toned mound" designated with yellow arrow is same shown in Mastcam image. HiRISE scene is ~3 km across.

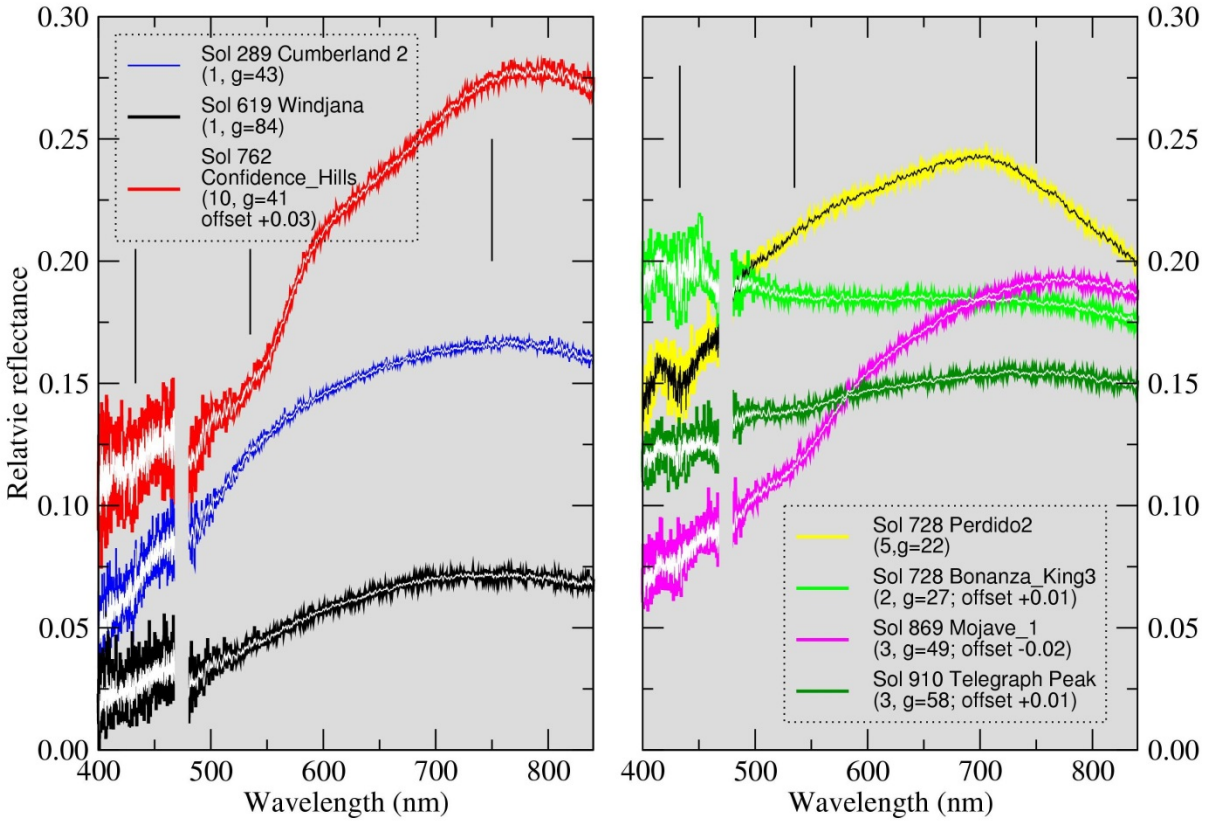

856

857 **Figure 10.** ChemCam relative reflectance spectra of representative locations for drill tailings
858 and fresh surfaces discussed here. Central white or black lines represent 5-channel average of
859 spectra shown in colors. Parenthetical notes refer to raster location number and phase angle of
860 observation (*g*). See Table 1 for details. Missing 468-480 nm data is region between ChemCam
861 detectors. Some spectra are offset for clarity, as shown in legend. Vertical bars correspond to
862 reference wavelength locations 433, 535, and 750 nm.

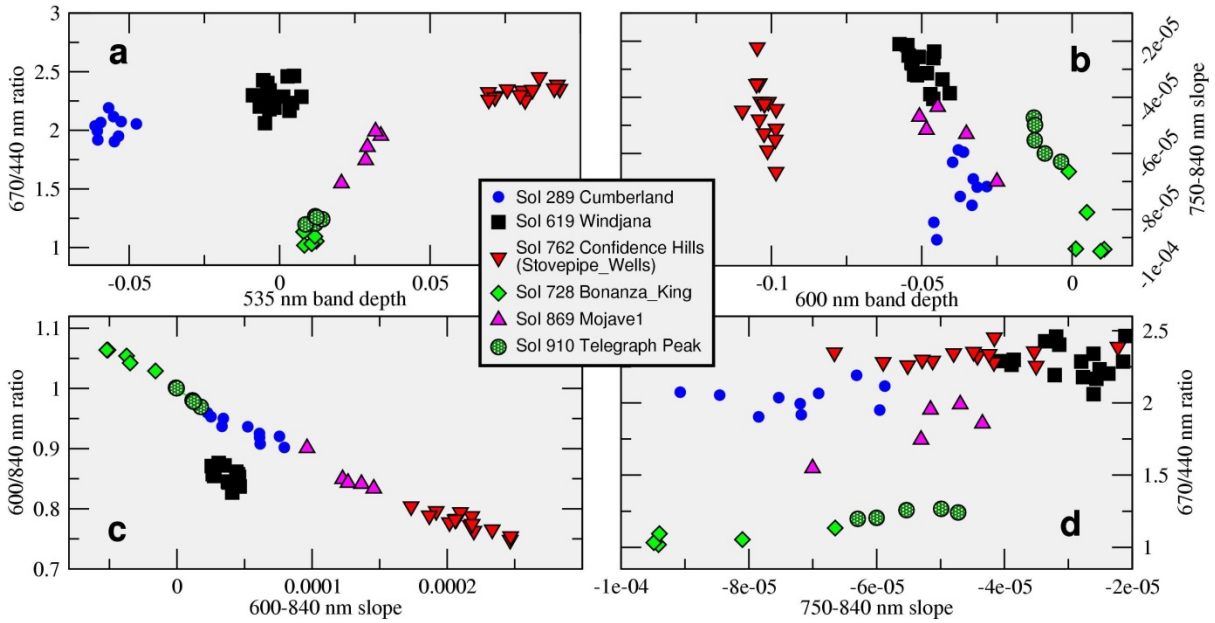

Figure 11. Spectral parameter comparisons for all drill tailing spectra. Not plotted is Perdido2 location #5, whose values of 750-840 nm slope ($-3.5e^{-4}$), 600/840 nm ratio (1.14), and 600-840 nm slope ($-1.1e^{-4}$) fall well outside the ranges plotted here.

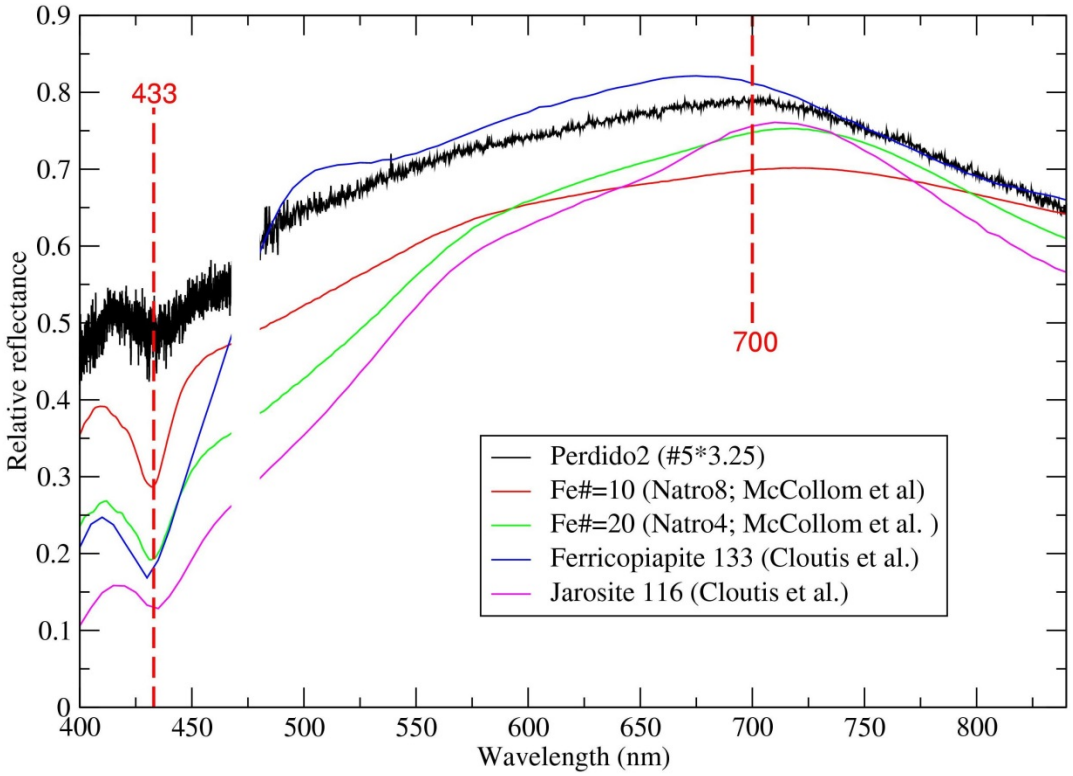

Figure 12. ChemCam passive spectrum of Perdido2 location #5 multiplied by 3.25 to facilitate comparison to laboratory spectra. Missing 468-480 nm data represents region between ChemCam detectors. Jarosite and ferricopiapite are from Cloutis et al. (2006) and synthetic natroalunite samples with small Fe# [= 100 × Fe/(Al+Fe), molar basis] are from McCollom et al. (2014). The absorption near 433 nm, reflectance downturn shortward of 410 nm, and reflectance downturn longward of 700 nm in Perdido2 are consistent with the presence of these types of iron sulfate minerals.

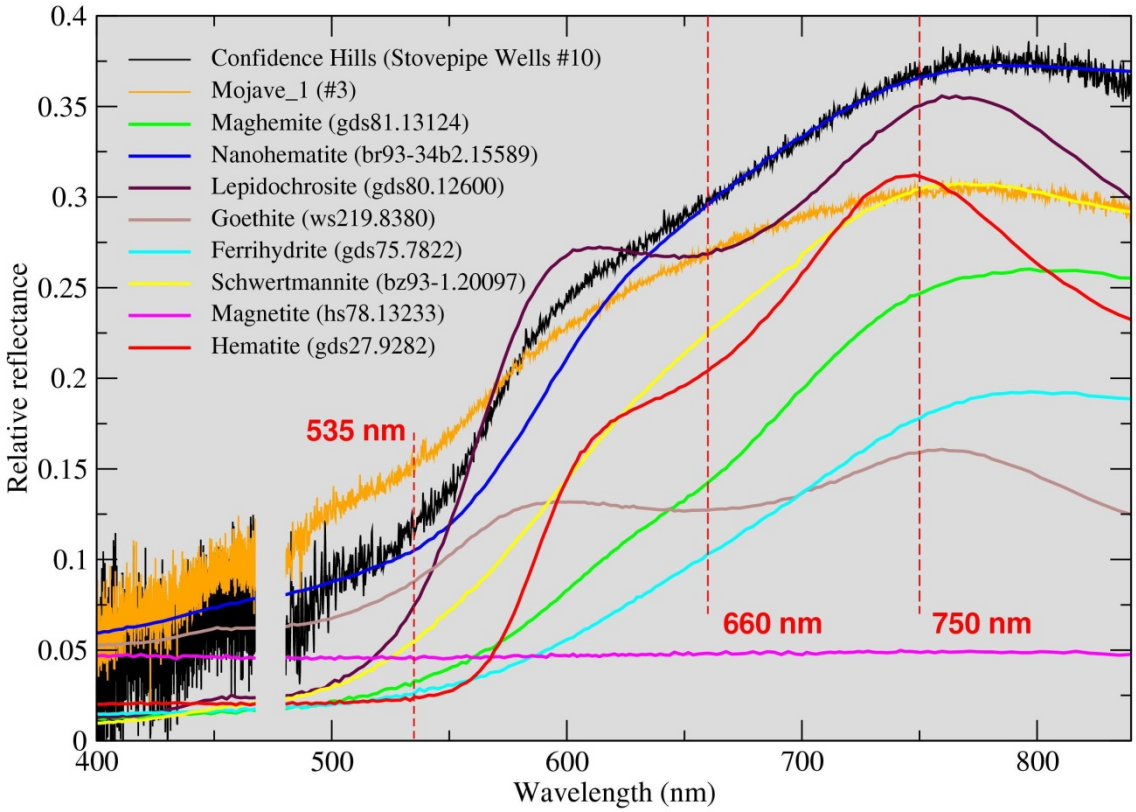

876

877 **Figure 13.** ChemCam passive spectra of Confidence Hills (Stovepipe Wells target location #10
878 from Figure 8) and Mojave drill tailings, contrast enhanced to facilitate comparison to laboratory
879 spectra of iron oxides. Missing 468-480 nm data represents region between ChemCam detectors.
880 Laboratory spectra are from USGS database (Clark et al. 2003). The combination of a broad
881 absorption near 535 nm, the flat, linear increase through the 660 nm region, and a decrease in
882 reflectance longward of 750 nm suggest the presence of a combination of crystalline and/or
883 nanophase hematite and a hydroxylated ferric phase like goethite or lepidocrocite.

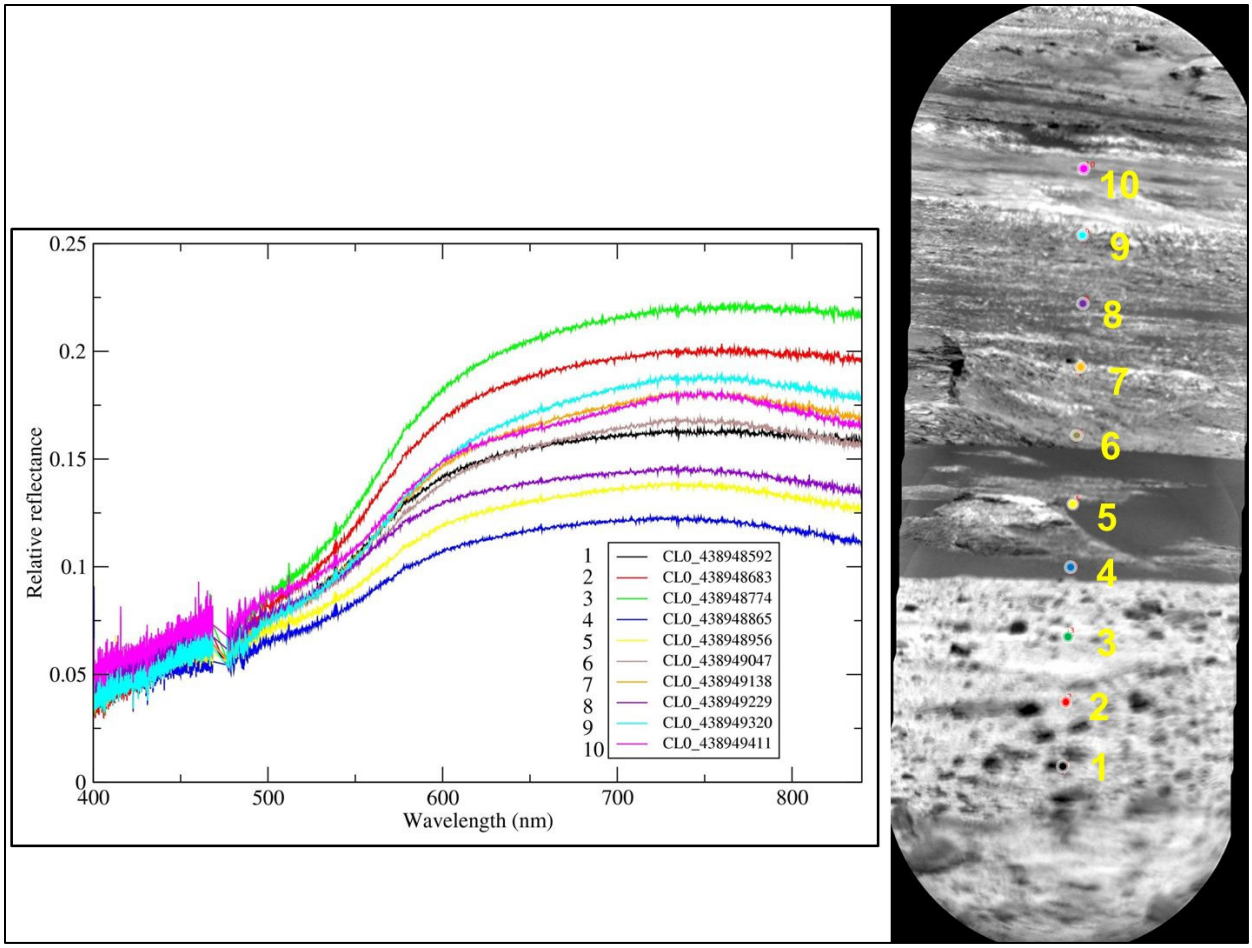

Figure 14a. ChemCam relative reflectance spectra (*left*) of Hematite Ridge 1 (HR1) area (cf. Figure 8) acquired on Sol 467 numbered according to acquisition locations shown in RMI mosaic (*right*). Colored points are located at approximate position and size of passive spectra fields-of-view, and color-coded to those in the spectral plot. Locations on Hematite Ridge (#6,7, 9, 10) show steep fall-off > ~747 nm, a weak band near 670 nm, and higher 535 nm band depth, consistent with hematite. Dark dune materials (locations #4,5,8) exhibit gradual fall-off > 750 nm consistent with olivine/pyroxene-bearing basaltic materials. Legend numbers correspond to spacecraft clock time used in CL0* filenames.

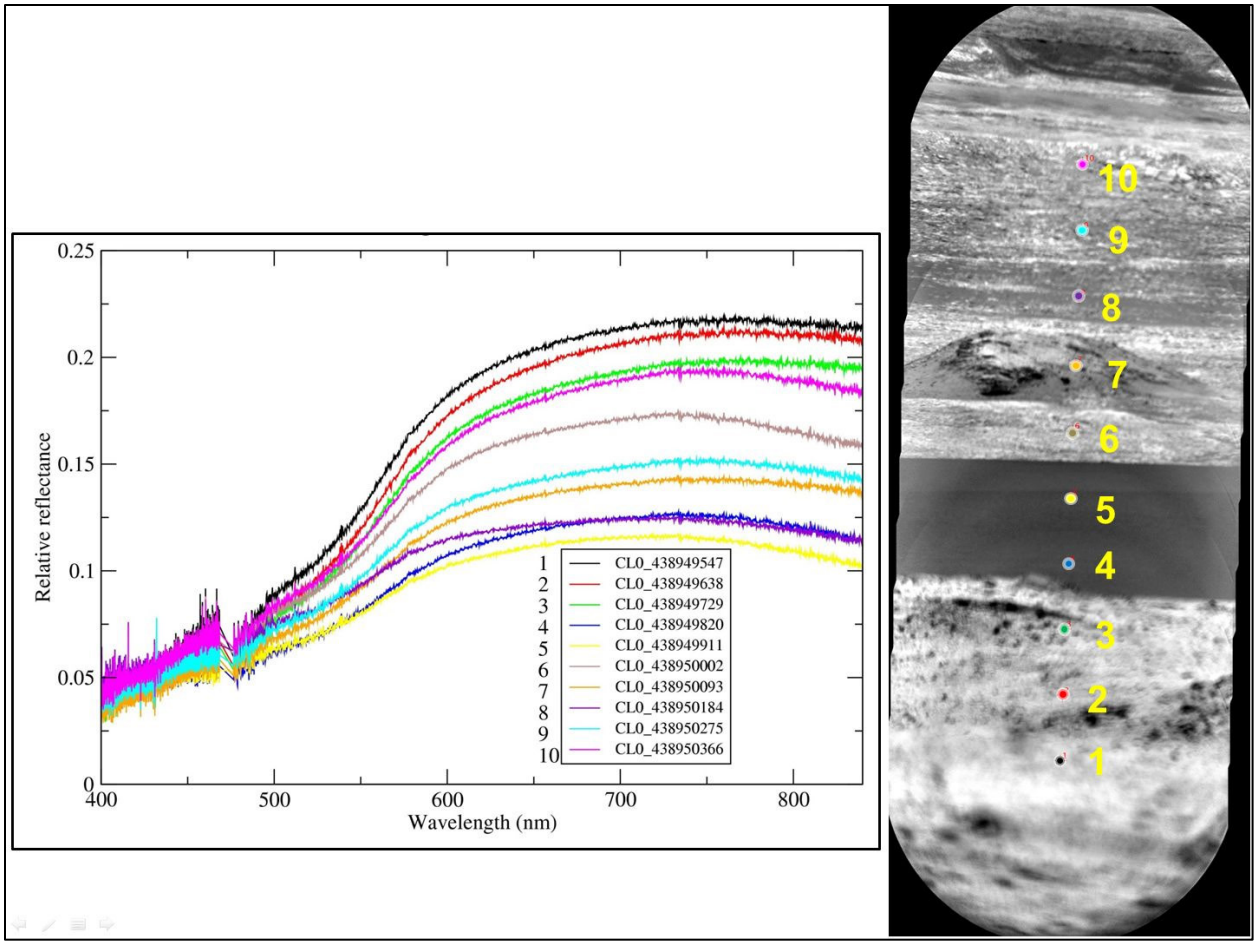

Figure 14b. ChemCam relative reflectance spectra (*left*) of Hematite Ridge 2 (HR2) area (cf. Figure 8) acquired on Sol 467 numbered according to acquisition locations shown in RMI mosaic (*right*). Colored points are located at approximate position and size of passive spectra fields-of-view, and color-coded to those in the spectral plot. Locations on Hematite Ridge (#6, #10) show steep fall-off > ~747 nm, a weak band near 670 nm, and higher 535 nm band depth, consistent with hematite. Dark dune materials (locations #4,5,8) exhibit gradual fall-off > 750 nm consistent with olivine/pyroxene-bearing basaltic materials. Legend numbers correspond to spacecraft clock time used in CL0* filenames.

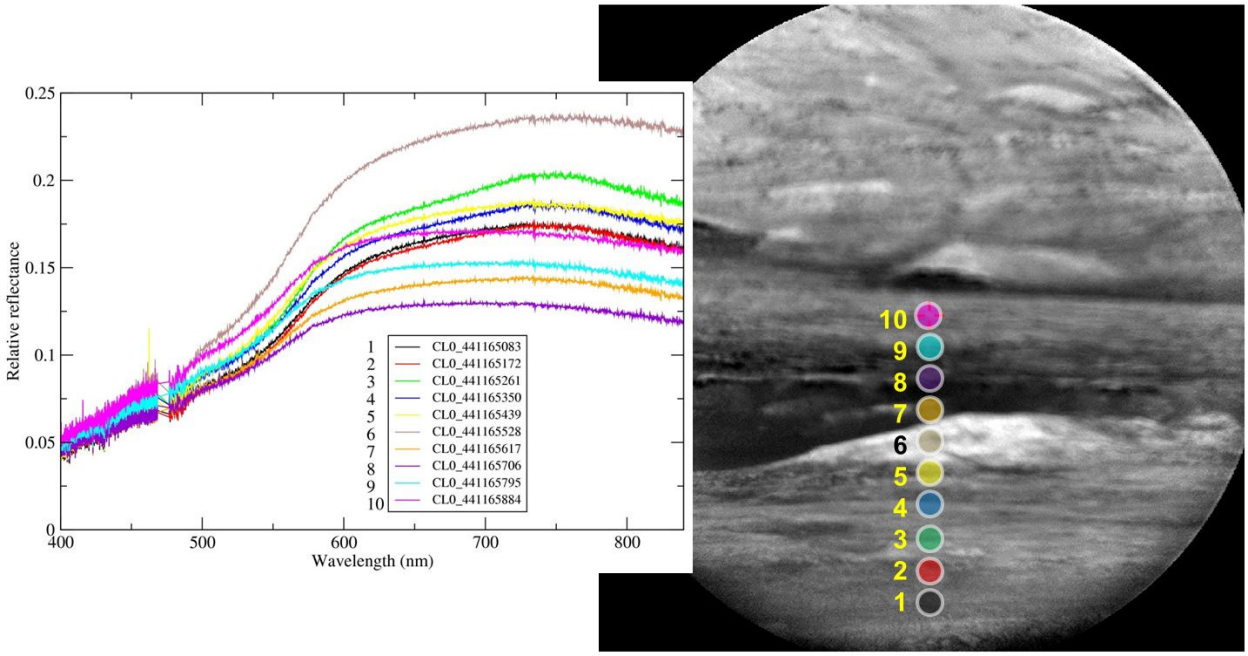

Figure 15. Sol 492 ChemCam passive spectra from raster HR5 acquired on Sol 492 and corresponding RMI image (CR0_441165845EDR_F0240408CCAM01492M1) of light-toned mound circled in Fig. 9. Colored points are located at approximate position and size of passive spectra fields-of-view, and color-coded to those in the spectral plot. Hematite-bearing regions are present on locations #3-5 (Hematite Ridge). Dark dune materials are present at locations #7-9, and location #10 on the "fan" materials exhibits similar spectral features at higher relative reflectance. Location #6 hit the light-toned mound but reveals few diagnostic spectral features in this wavelength range.

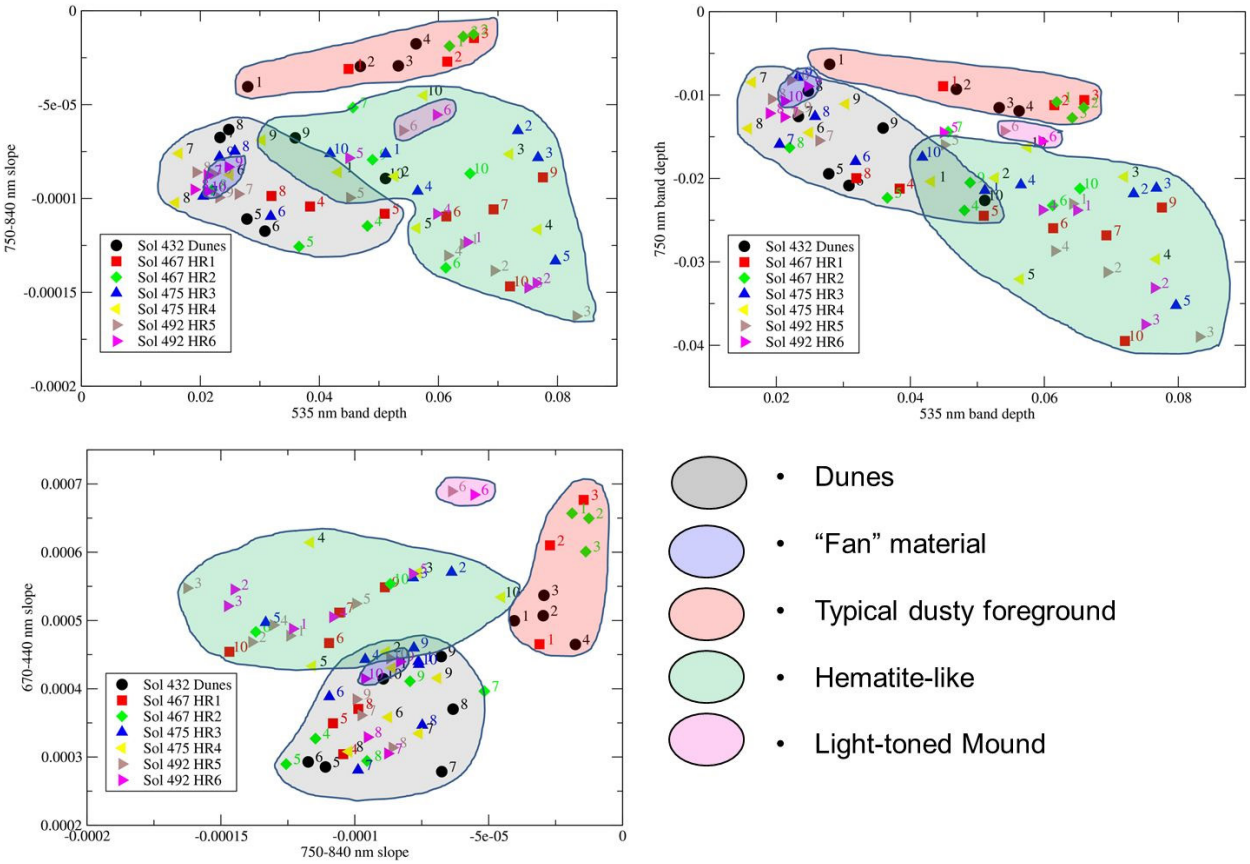

912

913 **Figure 16.** Representative spectral parameter plots for long-distance ChemCam passive spectra
914 (Table 1). Location numbers for each raster shown next to symbols (color-coded by
915 observation). Polygons show generalized spectral parameter regions associated with typical
916 dusty foreground materials, dunes, materials on the "fan" unit, the light-toned mound material
917 (Sol 492), and hematite-like spectra on or near Hematite Ridge.

918